AN ABSTRACT OF THE THESIS OF

Jae-Kyung Han for the degree of Master of Science in Materials Science presented on November 25, 2019

Title: Synthesis of Heterostructured Aluminum-magnesium System with Extreme Specific Strength Through the Application of High-pressure Torsion

Abstract approved:

_____

Megumi Kawasaki

Processing of metals through the application of high-pressure torsion (HPT) provides significant grain refinement in bulk metals at ambient temperatures. The ultrafine-grained (UFG) materials processed by HPT generally demonstrate the superior physical and mechanical characteristics. For utilizing the benefit of HPT, the feasibility of conventional HPT processing was demonstrated recently for the synthesis of bulk hybrid metals and alloys for a short period of time at room temperature. In the present study, the production of an Al-Mg nanostructured hybrid system was demonstrated by mechanical bonding of separate Al and Mg by means of HPT under a compressive pressure of 6.0 GPa for up to 60 turns at room temperature. A series of analyses were performed to examine the evolution of microstructure and mechanical properties and to evaluate the feasibility of HPT processing. The results demonstrate a significant opportunity for making use of HPT for the solid-state reaction of dissimilar metals to synthesize hybrid engineering materials consisting of intermetallic-based metal matrix nanocomposites (MMNC) and/or supersaturated solid solutions.

Synthesis of Heterostructured Aluminum-magnesium System with Extreme Specific Strength Through the Application of High-pressure Torsion

by
Jae-Kyung Han

A THESIS

submitted to

Oregon State University

in partial fulfillment of
the requirements for the
degree of

Master of Science

Presented November 25, 2019
Commencement June 2020

Master of Science thesis of Jae-Kyung Han presented on November 25, 2019

APPROVED:

Major Professor, representing Materials Science

Director of the Materials Science Program

Dean of the Graduate School

I understand that my thesis will become part of the permanent collection of Oregon State University libraries. My signature below authorizes release of my thesis to any reader upon request.

Jae-Kyung Han, Author

ACKNOWLEDGEMENTS

I would like to express my sincere gratitude to my advisor, Prof. Megumi Kawasaki, for all the guidance, advice and support throughout this study. I was fortunate to have a chance to join in her research group and successfully finish my study.

I would also like to thank my graduate committee members for their support and all the graduate students and professors who have helped me to conduct experiments, solve problems which lead me to the right direction by their generous support.

TABLE OF CONTENTS

Page

1. Introduction...…… 1

2. Literature Review……. 3

2.1 Grain refinement & Ultrafine grained materials…… 3

2.2 Severe plastic deformation …….……4

2.2.1 Classification of severe plastic deformation……...4

2.2.2 History and principle of high-pressure torsion……6

2.2.3 Paradox of strength and ductility…….…….12

2.3 Bulk-state reaction of dissimilar metals……..……..……14

2.3.1 Formation of hybrid nanostructured materials……..……14

2.3.2 Architecturing of hybrid materials by HPT…….……..……15

3. Experimental procedures…….……18

3.1 Materials and sample preparation……..……...……18

3.2 Materials processing…...……..……18

3.3 Microstructural analysis…….……...……...20

3.4 Mechanical properties.…….……22

4. Results ……23

4.1 Formation of metal matrix nanocomposite (MMNC)……..……23

4.1.1 Overview of microstructure in an Al-Mg alloy system……..…....23

4.1.2 Microstructural characterization of an Al-based MMNC…….....……24

4.1.3 Exceptional hardness in the Al-based MMNC…….……...….32

TABLE OF CONTENTS (Continued)

Page

4.2 Enhancement of solid-state reaction by parameter control…..……34

4.2.1 Effect of a torsional strain on mechanical bonding……...……34

4.2.2 Size effect on a mechanical bonding…….....……39

5. Discussion……46

5.1 Strengthening mechanisms in MMNCs……...……..……46

5.2 Strength-to-weight ratio of mechanically-bonded Al-Mg……..……48

5.3 Severe mixture of dissimilar metals during HPT…...…..……..……50

6. Summary and conclusions…….…….……..54

7. Future work…….……...…….……..57

Bibliography……...…….……..58

LIST OF FIGURES

Figure Page

Figure 2.2.1 Schematic illustration of ECAP [2]……..…..…….……5

Figure 2.2.2 Schematic illustration of HPT for (a) unconstrained and (b,c) constrained conditions [47]……..…….…....7

Figure 2.2.3 Schematic illustration of HPT machine [48]…….……...….8

Figure 2.2.4 Distribution of effective strain across the vertical cross-section of disks after HPT for 1 turn at 1.5 GPa under different constraining conditions [31]……..9

Figure 2.2.5 (a) Color-coded hardness contour maps for Al-1050 after HPT for 1/4, 1 and 5 turns under 6.0 GPa [51] and (b) hardness variation along the disk diameters of ZK60A after HPT for 0, 1/4, 1/2, 1, 3 and 5 turns under 6.0 GPa; the lower dashed line indicates the Vickers microhardness value of ~72 in the as-extruded condition without HPT and the error bars are at the 95% confidence level [52].…….11

Figure 2.2.6 The diagram showing the strength–ductility paradox as developed by Valiev *et al.*[54] where the shaded area represents the conventional behavior, the region of high strength and high ductility lies to the right of the solid and broken line and the numbers marked with percentages denote the reduction in thickness after rolling: the results for the Al–7%Si alloy are superimposed on the plot and the displacement to the right with increasing number of HPT turns, N, is indicated by the arrow [62]……..…13

Figure 2.3.1 Schematic illustration of roll cladding process [64]…...…….….14

Figure 2.3.2 (a) Schematic illustration of HPT processing and (b) shape of Al–Cu sample before HPT and after HPT for 100 turns [72]…...……16

Figure 2.3.3. Computational model for the HPT-processed hybrid sample showing the spiral structure [73]……..……..…….…..……17

Figure 3.2.1 A photograph of the HPT facility at OSU……..……..……..…..19

Figure 3.2.2 Schematic drawings of (a) a sample set-up for 10 mm diameter disks, (b) HPT processing for the mechanical bonding, and (c) a sample set-up for 25 mm diameter disks [79]…...……..……...……...…….20

LIST OF FIGURES (Continued)

Figure Page

Figure 4.1.1 The optical micrographs on cross-sectional planes of the Al–Mg system after HPT under 6.0 GPa at RT for, from the top, 1, 5, 10, 20 turns and for 20 HPT turns followed by PDA [93]…….…….……23

Figure 4.1.2 Representative TEM bright-field images showing (a) a layered microstructure consisting of the Al matrix region with one visible Mg phase, (b) a representative ultrafine grain in the Al matrix and (c) a dark-field image and the corresponding compositional maps of Al and Mg taken at the disk edge after HPT for 5 turns [74] and (d) XRD profiles showing, in ascending order, ZK60A, Al-1050 and the Al–Mg disks after HPT for 5 turns under 6.0 GPa [76]...…….…....25

Figure 4.1.3 (a) A representative bright-field image, (b) a dark-field image and the corresponding compositional maps of Al and Mg, (c) a high resolution TEM image taken in the Al matrix and (d) XRD profile in black and the simulated line profile in red at the edge of the Al-Mg system after HPT for 10 turns [74]……..……...27

Figure 4.1.4 (a) and (b) Representative TEM bright-field images, (c) the corresponding diffraction ring patters taken at the equiaxed microstructural region, (d) a dark-field image and the corresponding compositional maps of Al and Mg, and (e) XRD profile taken at the disk edge of the Al-Mg system after HPT for 20 turns [77]……....29

Figure 4.1.5 (a) A representative TEM bright-field image, (b) a high-resolution TEM image, (c) a dark-field image and the corresponding compositional maps of Al and Mg, and (d) XRD profile taken at the disk edge of the Al-Mg system after HPT for 20 turns followed by PDA [77]…….……...……..31

Figure 4.1.6 (a) Color-coded hardness contour maps taken at the vertical cross-section and (b) hardness variation along the disk diameter of the Al-Mg system after HPT for 1, 5, 10 and 20 turns and after HPT for 20 turns followed by PDA [82]……..33

Figure 4.2.1 (a) Overview of the cross-sections and the corresponding hardness color contour maps for the Al-Mg system after HPT for 40 (upper) and 60 turns (lower), (b) hardness variation along the disk diameters at the mid-thickness on the cross-sections of the Al-Mg disks after HPT for up to 60 turns [78]…….……..35

Figure 4.2.2 XRD line profiles taken at the disk edge of the Al-Mg disks after HPT for 40 (lower) and 60 turns (upper) by μXRD [78…..]….....…….……..37

LIST OF FIGURES (Continued)

Figure Page

Figure 4.2.3 (a) Cross-sectional micrographs and the corresponding hardness color contour maps for the Al-Mg disks with 25 mm diameter after HPT for 10 turns (upper) and 20 turns (lower) under 1.0 GPa at 0.4 rpm, and (b) the hardness valuation with the standard error along the disk diameter for these two mechanically-bonded Al-Mg disks [79]...…….……..39

Figure 4.2.4 (a) A representative TEM bright-field image, (b) the corresponding selected area electron diffraction (SAED) pattern and (c) a dark-field image and the corresponding element mapping taken at the disk edge at r ≈ 10 mm after HPT for 20 turns under 1.0 GPa at 0.4 rpm [79]……...…….…….….41

Figure 4.2.5 (a) XRD profiles conducted by μXRD at three different locations of near-center, mid-radius and edge of the Al-Mg disks with 25 mm diameter after HPT for (a) 10 and (b) 20 turns [79]……...……...……...42

Figure 4.2.6 Conventional Williamson-Hall plots for the Al-Mg system with 25 mm diameter after HPT for (a) 10 and (b) 20 turns under 1.0 GPa at 0.4 rpm [79]……....44

Figure 5.1.1 Estimated Vickers microhardness values with increasing Mg content in Al matrix of the Al-Mg system with 10 mm diameter after HPT for 10 turns; the red squares with error bar denotes the estimated total hardness, and the increase in hardness induced by three different strengthening mechanisms of solid solution strengthening [109,110], HP strengthening [110] and precipitation strengthening [112] are denoted by the blue upright triangles, green circles and pink inverted triangles with error bars, respectively [74]……..……47

Figure 5.3.1 A relationship between r_b and the estimated shear strain and equivalent strain for both Al-Mg and Al-Cu systems after HPT for up to 60 turns and up to 40 turns, respectively, under 6.0 GPa for 1.0 rpm at RT [78]…….……...……...51

LIST OF TABLES

Table Page

Table 1 Summary of estimated lattice parameter of Al, the Mg concentration in the Al matrix, the coherent crystallite size, and the micro-strain for the disk edges of the Al-Mg system with 10 mm diameter after HPT for 40 and 60 turns [78]……..…..…...38

Table 2 The results on compositional analysis by MAUD based on the XRD patterns shown in Fig. 4.2.5 [79]…….…….....…..43

Table 3 Summary of estimated lattice parameter of Al, the Mg concentration in the Al matrix, the micro-strain and the crystallite size for different measurement locations of center, mid-radius and edge of the Al-Mg disks with 25 mm diameter [29].……...44

Table 4 The measured density, the maximum Vickers microhardness value, and the estimated strength-to-weight ratio for the MMNCs in the Al-Mg system after HPT for 5-20 turns, and the reference materials of Al-1050 and ZK60A alloys after 5 HPT turns [119]……...……..…….…….……..49

1. Introduction

To meet our increasing demands, metallic materials with high specific strength and good ductility are indispensable for structural applications [1]. Several non-ferrous alloys are considered as a good candidate for replacing the ferrous metals due to a light-weight and thus good strength-to-weight ratios. However, the improvement in these properties becomes an urgent issue under the current energy crisis. Among the various processing methods applied to improve the mechanical properties and additional functionalities, processing of metals through the application of severe plastic deformation (SPD) [2-4] has attracted much attention as a potential technique for achieving ultrafine-grained (UFG) materials which are referred as interface-controlled materials through the special arrangement and control of grain boundaries [4] which lead to significant changes in their mechanical responses.

Within a numerous number of the reported SPD techniques, high-pressure torsion (HPT) [5] has defined as one of the most powerful techniques [6] for achieving true nanostructures within a disk-shaped bulk material by imposing very high torsional strain under compressive pressure. A unique feature of such ultrafine-grained metals is that there is a potential to improve both strength and ductility, while it is uncommon when considering the paradox of strength and ductility where most materials are either strong but brittle or simply soft without strength. In practice, an example shown in an earlier report demonstrated the strengthening of an aerospace-grade Al-7075 alloy after HPT processing while maintaining reasonable formability [7]. Moreover, HPT processing demonstrated successful deformation of hard-to-deform materials such as Mg alloys [8] and bulk intermetallic compounds [9-12] even at room temperature (RT). However, it has been described that there is a saturation in grain refinement and thus it results in an upper limit of improving the mechanical properties in metals and alloys, by grain refinement [13]. Therefore, there is a difficulty for achieving superior properties by a single SPD technique unless additional processing is applied to the as-processed materials [14,15].

Numerous point and line defects are introduced during HPT processing which accommodate the significant grain refinement and furthermore accelerate the atomic mobility even at room temperatures [16]. Therefore, HPT has been applied for the bonding of machining chips [17-20] and the consolidation of metallic powders [21-30] in recent years. Nevertheless, these processes often require high processing temperature and/or two-step processes for powder compaction prior to HPT processing to avoid the damage on anvils.

Accordingly, a new approach of solid-state reaction by applying conventional HPT processing has been developed for the mechanical bonding of dissimilar metals at room temperatures in the past five years. The goal of this approach is to improve the mechanical properties and lightweighting of materials by the bonding of dissimilar metals. Thus, in this study, mechanical bonding of dissimilar metals of Al and Mg is conducted by applying HPT having a unique sample set-up at room temperature. A series of characterizations are conducted to show the microstructural evolution and enhanced mechanical properties of the synthesized Al-Mg hybrid materials after HPT up to 60 turns. Specifically, analyses evaluated a severe mixture of dissimilar metals, mechanisms of the improved strength, and strength-to-weight ratio of the mechanically bonded Al-Mg system. A special emphasis is placed on evaluating the feasibility of the mechanical bonding through HPT for scaling-up the samples size.

2. Literature Review

2.1 Grain refinement & Ultrafine grained materials

Numerous numbers of studies have been conducted on grain refinement of crystalline materials to improve mechanical properties to meet the increasing demands. Among mechanical properties, strength and ductility are considered as the most important properties for the structural materials. In general, these properties depend on the microstructure of the material and are highly affected by grain size. At low temperatures, typically at temperatures below ~0.5 T_m where T_m is the absolute melting temperature, most metals follow a relationship suggested by Hall and Petch [31,32] describing a correlation between yield stress, σ_y, and the grain size, d, of the metal, which is given by the following form:

$$\sigma_y = \sigma_0 + k_y d^{-1/2} \qquad (1)$$

where σ_0 is the lattice friction stress and k_y is a yielding constant. Thus, eq. (1) implies that an increase in yield strength is induced by a reduction in grain size.

There are numerous advantages other than improvement in hardness when grain refinement is achieved to subgrain size and further down to nanoscale grains [33,34], such as enhanced strain rate sensitivity [35], better wear resistance [36,37] and improved electrical conductivity [38]. Therefore, there has been enormous studies to produce polycrystalline materials having small grain sizes, so called ultrafine-grained (UFG) materials. A term of UFG materials is first defined more than a decade ago [2] as polycrystals having an average grain size less than ~1 μm, specifically scale of submicrometer (100 nm - 1 μm). Moreover, further grain refinement produces a finer microstructure having true nanometer grain sizes (less than 100 nm), thereby production of bulk nanostructured materials (BNM). Bulk UFG materials are defined with additional criterion that the microstructure needs to be reasonably homogeneous with equiaxed grains having high-angle grain boundaries [2] which result in the advanced and unique properties of the materials [39].

2.2 Severe plastic deformation (SPD)

Over the last few decades, there has been extensive numbers of reports in the field of SPD to introduce bulk UFG/nanostructured materials for improving the mechanical properties which are not achievable due to a limitation of grain size reduction by the conventional thermo-mechanical processing including uniaxial tension and compression, extrusion, rolling and drawing. SPD processing refers to a technique of metal processing in which very high strain is imposed on materials and thereby achieving exceptional grain refinement which leads to superior mechanical and physical properties. The material is required to retain the overall dimensions reasonably after the process with imposing very high plastic strain. The special geometries of the SPD processing machines produce a significant hydrostatic pressure induced by prevention of free flow of the materials. This hydrostatic pressure is essential to introduce high imposed strain leading to the generation of high densities of points and lattice defects which resulted in the significant grain refinement [2].

2.2.1 Classification of severe plastic deformation

Numerous techniques are now available for SPD processing which enable to fabricate the UFG materials. Among the various SPD methods, equal-channel angular pressing (ECAP) and high-pressure torsion (HPT) are the most promising techniques to produce smaller grain sizes and larger fractions of high-angle grain boundaries than other SPD techniques [40,41]. In addition, there are accumulated roll-bonding (ARB), multi-directional forging (MDF), twist extrusion (TE) and others.

As illustrated in Fig. 2.2.1 [2], the principle of ECAP involves the pressing of a rod- or bar-shaped billet within a constrained channel which is bent at a specific angle [42].

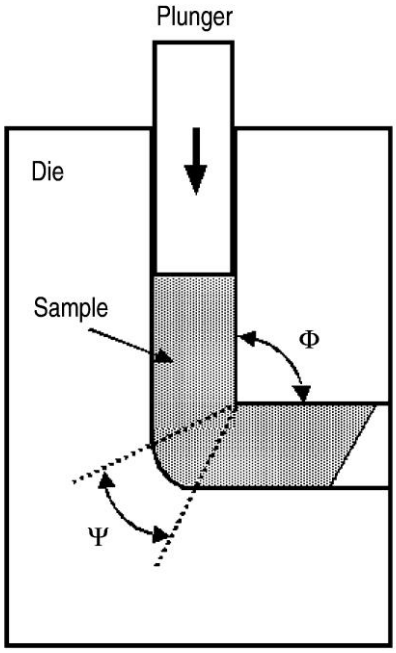

Figure 2.2.1 Schematic illustration of ECAP [2]

The billet receives a simple shear strain during the ECAP process only when the billet pass through intersection of the two channels. The equivalent strain, ε, applied to the billet after ECAP is given by the form [43],

$$\varepsilon = (N_E/\sqrt{3})[2\cot\{(\Phi/2) + (\Psi/2)\} + \Psi\mathrm{cosec}\{(\Phi/2) + (\Psi/2)\}] \quad (2)$$

where Φ is the angle between two parts of the channel and Ψ is the angle representing the outer arc of curvature at the intersection of two channel and N_E denotes the number of passes. The ECAP die has two channels with the same area of cross-section so that the multiple pass processing is available to induce higher strains leading ultimately to the formation of UFG materials.

The accumulated roll bonding (ARB) is first invented by Saito *et al.* [44] through a use of conventional rolling facility with a modification of sample preparation procedure. In practice, the ARB process includes several steps. A sheet metal is rolled with a thickness reduction of 50 % and then cut into two halves. These thinned and cut sheets are stacked after cleaning up the contact faces using a wire-

brushing for better bonding and then rolled again to achieve a thickness with a reduction of 50 %. Thus, multiple processing cycle attributes to the accumulation of a large strain to the sheet therefore producing an UFG structure. The ARB process introduces the equivalent strain varies with the number of cycles, N_{A}, given by $\varepsilon_{N_{\mathrm{A}}} = 0.80N_{\mathrm{A}}$ [44]. The grain morphology after ARB processing reveals a pancake-like structure elongated along a rolling direction instead of overall homogeneous microstructure with equiaxed grains. The produced materials thus often demonstrate an anisotropic mechanical response.

2.2.2 History and principle of high-pressure torsion

In 1940s, it was demonstrated by Bridgman that torsion tests under hydrostatic pressure attribute to increase in the fracture strain of the material [45] and this work is now considered as the first report of high-pressure torsion (HPT) where a history of HPT processing was summarized elsewhere [46]. The principles of the HPT are well defined in an earlier review report [5]. Specifically, a thin disk-shaped material is placed between the upper and lower anvils, and then large torsional straining is subjected to the disk by the rotation of the bottom anvil while high hydrostatic pressure is applied during the process.

The anvil set-up for HPT has been developed with three different types of processing, namely unconstrained, constrained and quasi-constrained HPT, and these are well described with figures in an earlier report where these three anvil configurations are shown in Fig. 2.2.2 [47].

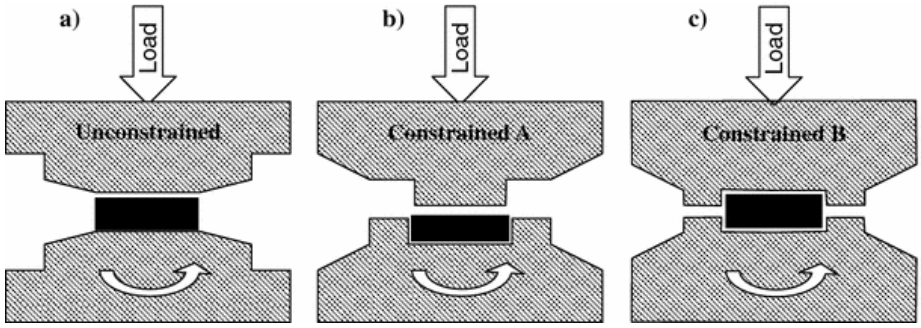

Figure 2.2.2 Schematic illustration of HPT for (a) unconstrained and (b,c) constrained conditions [47]

The HPT processing was first developed with the anvils having an unconstrained condition in which, as shown in Fig. 2.2.2(a), the disk sample flow out freely during torsional straining under high pressure. Therefore, there is a continuous decrease in the thickness of materials during HPT processing, especially in peripheral regions, and a shape of the disk is poorly defined. Due to the drawback of the unconstrained HPT, constrained HPT has developed for processing where there is a hollow cylinder wall covering the anvil set and a sample so that the disk sample is deformed while the procedure reasonably maintains the dimension of the disk. However, the material flow out into the gap between the cylinder wall and the anvils due to the inevitable tolerance. In addition, huge friction is generated between the sample and the cylinder wall resulting in an unintended heat generation, and thus the processed material receives inhomogeneous deformation and a resultant heterogeneous microstructure. Therefore, a quasi-constrained HPT set-up was developed to overcome the disadvantages of these two types of anvil set-ups and a schematic illustration of the anvil set-up for quasi-constrained HPT is shown in Fig. 2.2.3 [48].

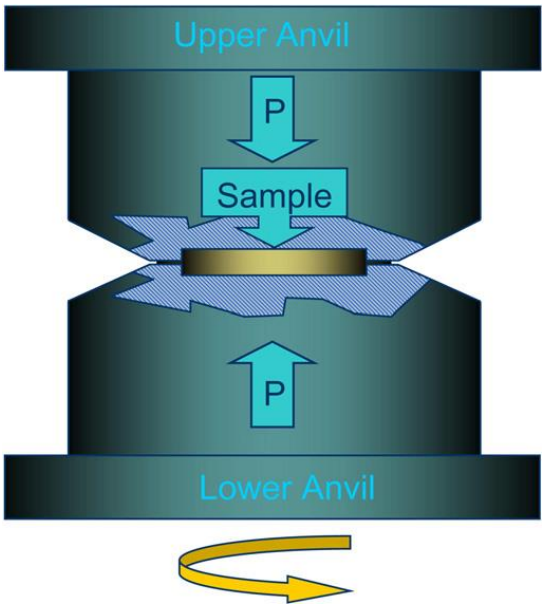

Figure 2.2.3 Schematic illustration of HPT machine [48]

The disk is placed within a cavity of the lower and upper anvils and this geometry has an advantage to apply higher pressure. The initial thickness of the sample should be thicker than the sum of the depths of the cavities to prevent a direct contact of the anvils which causes a failure of the anvils. Thus, a small amount of the materials flows out into a small gap between the anvil set mostly during loading of compressive pressure and an early stage of the torsional straining so that the hydrostatic pressure is generated due to a back pressure induced in the area marked as grey color in the illustration [48]. However, the quasi-constrained HPT requires a well-aligned anvil set because the central axis of the anvil set is not fixed unlike the constrained HPT. The finite element simulation computed the induced effective strain with the anticipated sample shapes for these three different types of the HPT anvil configurations and the results are shown in Fig. 2.2.4 where HPT processing was simulated under an applied pressure, *P*, of 1.5 GPa for one revolution with a rotational speed of 1.0 rpm [49].

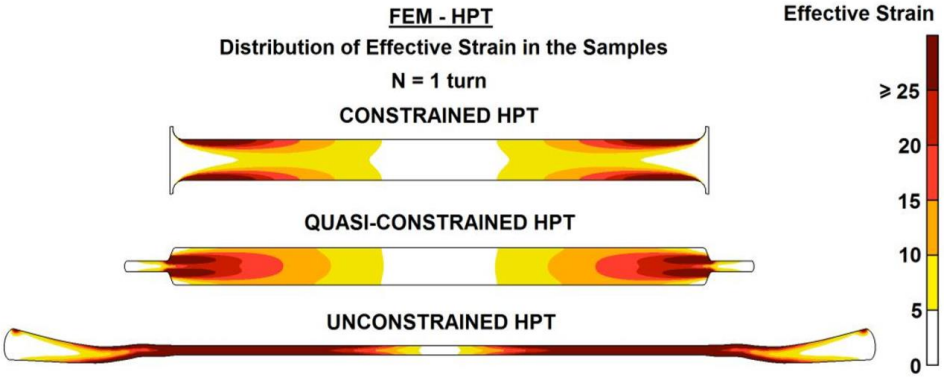

Figure 2.2.4 Distribution of effective strain across the vertical cross-section of disks after HPT for 1 turn at 1.5 GPa under different constraining conditions [31]

For constrained HPT, the sample received highest strain at a limited region near surfaces at the peripheral regions of the disk whereas almost zero strain applied at a large volume at the disk center. On the other hand, the unconstrained HPT set-up reveals high straining but instead a significant loss of sample volume. Unlike these two set-ups, the quasi-constrained HPT set-up demonstrates a reasonably homogeneous distribution of effective strain at the disk periphery after 1 HPT turn while maintaining the initial thickness and shape of the materials during the process.

The imposed shear strain, γ, during the torsional straining can be calculated by the following relationship for the quasi-constrained HPT condition [49],

$$\gamma = \frac{2\pi N r}{h} \qquad (3)$$

where N is the number of revolutions, r is the distance from the center of the disk, and h is the disk thickness. An earlier paper considered the imposed straining by considering a change in the disk height during HPT processing [49]. Nevertheless, using the relation between shear strain and equivalent strain, von Mises equivalent strain is described in the following form [50]:

$$\varepsilon_{\mathrm{eq}} = \frac{2\pi N r}{h\sqrt{3}} \qquad (4)$$

These equations imply that the imposed strain increases when the number of revolutions increases, the distance from the disk center increases, and the thickness of the disk decreases while the minimum thickness of the disk sample should be more than the total depth of a pair of the anvil cavities. Therefore, the maximum applied strain is achieved at the disk edge and it decreases toward the center of the disk, and theoretically the imposed strain is zero at the disk center. As a result, it is difficult to achieve a homogeneous microstructure within a disk. However, numerous researchers have been reported firm experimental results to achieve reasonably homogeneous microstructure when reasonably high strain is introduced by increasing numbers of HPT turns to materials.

For better explanation, there are two earlier reports showing the significance of increasing numbers of HPT turns to achieve a homogeneous microstructure, thus demonstrating homogeneous hardness across the disk diameters of Al and Mg alloys. Figure 2.2.5 represents (a) the overall hardness distribution on the surfaces of an Al-1050 alloy processed by HPT under 6.0 GPa for 1/4, 1 and 5 turns [51] and (b) the hardness variations with error bars measured at near mid-sections along the disk diameter of a ZK60A alloy processed by HPT up to 5 turns under 6.0 GPa and the lower dashed line denotes the hardness value of the as-extruded ZK60A [52].

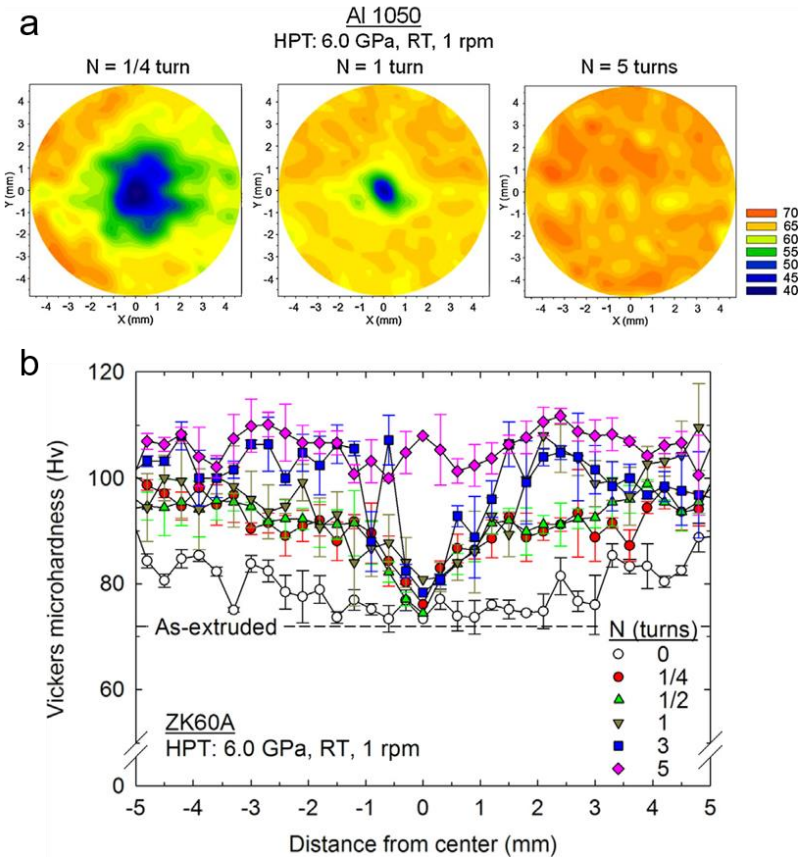

Figure 2.2.5 (a) Color-coded hardness contour maps for Al-1050 after HPT for 1/4, 1 and 5 turns under 6.0 GPa [51] and (b) hardness variation along the disk diameters of ZK60A after HPT for 0, 1/4, 1/2, 1, 3 and 5 turns under 6.0 GPa; the lower dashed line indicates the Vickers microhardness value of ~72 in the as-extruded condition without HPT and the error bars are at the 95% confidence level [52]

Since the microstructure significantly affects to the hardness of materials, the hardness measurements are commonly used to evaluate the evolution of microstructure through the HPT process. The hardness distributions for both Al and Mg alloys revealed a similar trend when the number of HPT turns increases. The hardness at the peripheral regions drastically increased and reached much higher than the disk center where there was almost no hardness evolution before and after 1/4 turn of HPT processing in Al-1050 and ZK60A alloys. After 1 turn of HPT, the high hardness at the disk edges slightly increased and the hardness at the disk central

regions remained consistent in both alloys. After 5 turns of HPT, the overall hardness values increased significantly in comparison with the materials prior to processing and the achieved high hardness become reasonably homogeneous along the diameter with the saturated Vickers microhardness values, Hv, of ~65 and ~110 for Al-1050 and ZK60A, respectively. Since both Al and Mg alloys exhibit the strain hardening behavior, it is possible to achieve homogenous hardness evolution throughout the disk and reasonably homogenous microstructure by applying higher torsional straining by increasing numbers of HPT turns [53].

2.2.3 Paradox of strength and ductility

UFG metals processed by SPD generally demonstrate higher strength than coarse-grained metals due to strengthening by grain refinement as expressed by eq. (1) whereas exhibiting very low ductility at ambient temperatures. This behavior of engineering metals is so called *paradox of strength and ductility* [54] which is appropriately defined as “materials may be strong or ductile, but rarely both at once” [55,56]. At ambient temperatures, a decrease in the ductility of UFG metals is mainly attributed to low strain hardening rate combined with low strain rate sensitivity, *m*, during plastic flow. Therefore, an important requirement for enhancing the ductility of UFG metals is to increase a rate of strain hardening to effectively block and accumulate the number of dislocations [3]. The onset of necking can be delayed so that the materials are able to exhibit reasonable levels of tensile ductility only if the high value of *m* is accompanied with the high value of strain hardening rate [57]. The grain boundaries become the sources for dislocations to sink without much accumulation when grain size becomes very small, so that the grain boundaries are no longer effective to accumulate the number of dislocations [58]. In this way, the rate of strain hardening become lower, thereby limiting the elongation of failure of the UFG materials [59-61]. The paradox of strength and ductility is presented in a plot of yield stress versus elongation to failure with the experimental datum points for Al and Cu with different cold-rolling amount red circles and blue squares, respectively, as shown

in 3.Fig. 2.2.6 [62]. Thus, as these reference materials show in the plot, most engineering materials after mechanical processing lie in the shaded area indicating that the materials show either high strength with low ductility or low strength with high ductility.

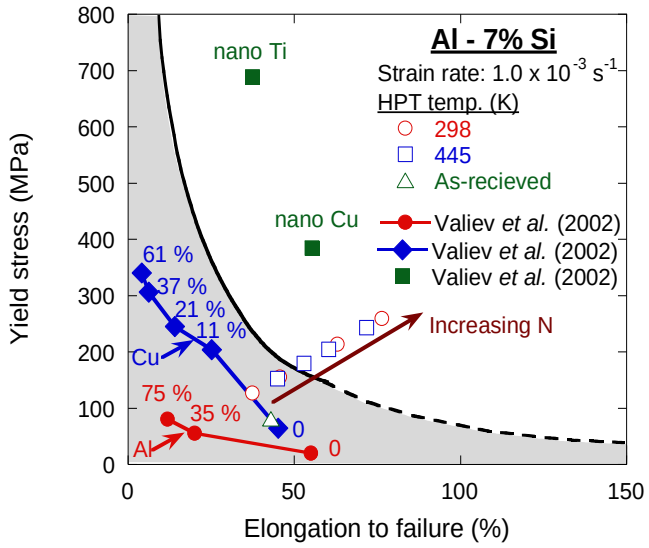

Figure 2.2.6 The diagram showing the strength–ductility paradox as developed by Valiev *et al.*[54] where the shaded area represents the conventional behavior, the region of high strength and high ductility lies to the right of the solid and broken line and the numbers marked with percentages denote the reduction in thickness after rolling: the results for the Al–7%Si alloy are superimposed on the plot and the displacement to the right with increasing number of HPT turns, *N*, is indicated by the arrow [62]

The points denoted as nano Cu and nano Ti indicate exceptional results to the paradox laying beyond the shaded area with excellent combinations of high strength and high ductility after processing through ECAP and HPT, respectively [54]. Also, the Al-7 % Si alloy after HPT processing reveals a clear trend of increase in both yield stress and ductility with increasing number of HPT turns at the processing temperatures of 298 and 445 K when testing at a strain rate of $1.0 \times 10^{-3} s^{-1}$ [62]. The enhancement of strength is due to the grain refinement and the exceptional

ductility is due to a transition of deformation mechanism from diffusion-controlled flow process to grain boundary sliding (GBS) [54,62]. The enhanced diffusivity by larger fraction of non-equilibrium grain boundaries introduced during SPD processing attributes to the activation of grain boundary sliding even at ambient temperatures. These experimental evidences demonstrate the feasibility of SPD to introduce UFG materials which overcome the *paradox of strength and ductility*, thereby achieving both high strength and excellent ductility even at ambient temperatures.

2.3. Bulk-state reaction of dissimilar metals

2.3.1 Formation of hybrid nanostructured materials

There are numerous reports demonstrating mechanical bonding of dissimilar metals with applying the conventional rolling procedure. Chang *et al*. [63] reported the fabrication of Mg/Al multilayers by cold-roll bonding of separate Al and Mg at ambient temperature. Thereafter, Macwan *et al.* [64] reported the fabrication of an Al/Mg/Al tri-layer by a clad-rolling process by means of a conventional rolling technique and a schematic illustration of this technique is shown in Fig. 2.3.1.

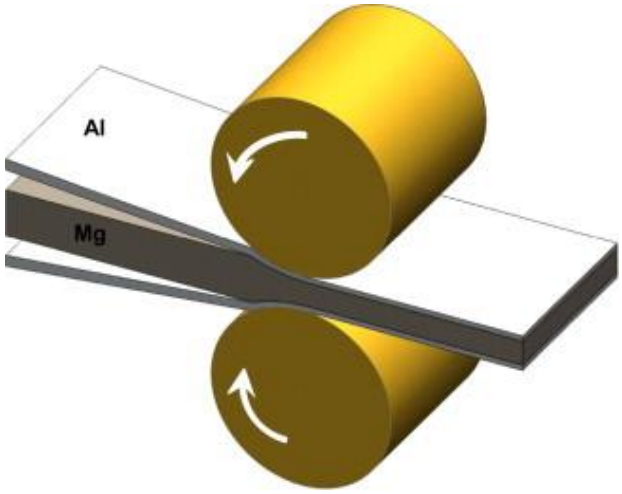

Figure 2.3.1 Schematic illustration of roll cladding process [64]

This study demonstrated Al-Mg layers in a good bonding condition without any voids and showed the improvement of mechanical properties such as ultimate tensile strength and elongation to failure. In order to achieve further grain refinement and enhance mechanical properties of alloy sheets, a series of dissimilar metals have been processed by the application of ARB for the Al-Cu [65, 66], Al-Mg [67-69] and Al-Zn [70] systems. The principle of this process is same with the ARB processing, but a difference is that stacking sheets of dissimilar metals were applied instead of one kind of metal and alloy. These studies demonstrated the increase in mechanical properties of the hybrid alloy sheets after ARB processing, but the ARB-processed fine-grained metals often fail to achieve homogeneous microstructure in all directions and show anisotropic plastic behaviors along the rolling direction and the through-thickness direction [71].

2.3.2 Architecturing of hybrid materials by HPT

In addition to cladding with an ARB process, several reports demonstrated recently the mechanical bonding of dissimilar metals through the application of HPT with a few different sample set-ups. Figure 2.3.2 shows one of the first reports demonstrating the solid-state reaction of Al and Cu where (a) a schematic drawing of a sample set-up prior to HPT and (b) the photos showing the shape of the sample before and after HPT processing [72].

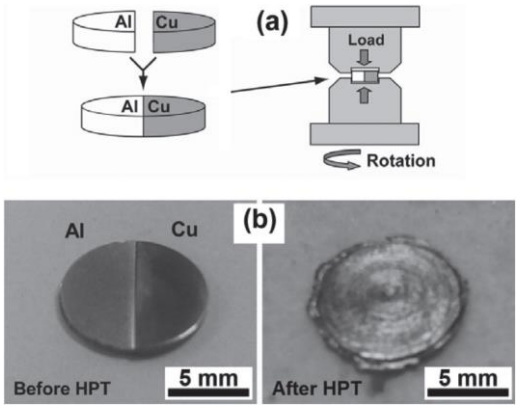

Figure 2.3.2 (a) Schematic illustration of HPT processing and (b) shape of Al–Cu sample before HPT and after HPT for 100 turns [72]

Two semi-circular disks of Al and Cu were placed in the lower anvil to delineate a complete disk shape and then processed by HPT for 100 turns at 6.0 GPa. A microstructural analysis demonstrated the formation of distorted Al-Cu lamellar structures with the nano-scale layers. Furthermore, the HPT processing for 100 turns induced a formation of two intermetallic compounds of Al_2Cu and Al_4Cu_9. The accelerated diffusion under high pressure and torsion processing attributes to the solid-state reaction of Al-Cu and formation of intermetallic compounds at room temperature. Another experimental and computational study was conducted for a similar but different sample set-up for architecturing a spiral structure and texture in an Al-Cu composite [73]. Figure 2.3.3 shows a result from computational modeling where the HPT-processed hybrid sample showing the spiral structure and the deformed Cu and Al alloys in separate figures. In practice, the four quarter-circular disks of an Al-6061 alloy and pure Cu were used for HPT processing at 2.5 GPa for 1 turn. This study demonstrated the potential for fabricating Al-Cu hybrid materials, however, there is no detailed microstructure information available.

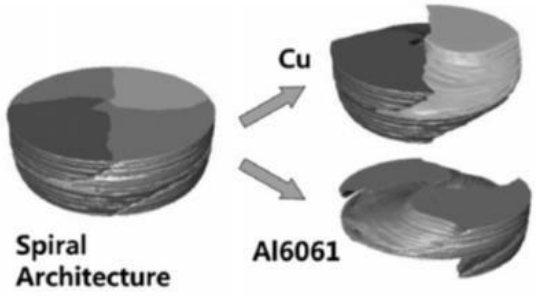

Figure 2.3.3. Computational model for the HPT-processed hybrid sample showing the spiral structure [73]

Following these preliminary studies, a simpler procedure is introduced for the direct bonding of dissimilar metals by mean of the conventional HPT process on Al and Mg by simply stacking two Al disks and Mg disk in the order of Al/Mg/Al without any surface treatment and this study was reported for publications [74-80]. This unique sample set-up of HPT processing has been applied for several different metal combinations such as Al/Cu/Al [81], Al/Fe/Al [82], Al/Ti/Al [82], Cu/Al/Cu [83], Cu/ZnO/Cu [84], Zn/Mg/Zn [85], Fe/V/Fe [86,87], and V-10Ti-5Cr/Zr-2.5Nb/V-10Ti-5Cr [88].

3. Experimental procedures

3.1 Materials and sample preparation

This study uses two sets of Al and Mg alloys. The first set includes a commercial purity aluminum, Al-1050, containing 0.40 wt.% Fe and 0.25 wt.% Si as major impurities and a ZK60A magnesium alloy containing 6.0 wt.% Zn and 0.72 wt.% Zr. The second set includes the consistent the Al-1050 aluminum alloy described above and a commercial AZ31 magnesium alloy containing 3 wt.% Al and 1 wt.% Zn.

Two different sample sizes are applied for grain refinement processing in this study. First, a standard specimen size with a diameter of 10 mm and thicknesses of ~0.80 mm is used for most of the experiments in this study. The first set of Al and Mg alloys were used for the experiments using the standard 10 mm diameter disks. Secondly, a scaled-up specimen having a disk diameter of 25 mm and thicknesses of ~2.5 mm was prepared for the evaluation of a possibility to scaling up of bulk nanocrystalline metals for application purposes. The second set of the Al and Mg alloys were applied for evaluating the scale-up processing.

For preparing the standard size disks, a plate of Al having a thickness of 1.2 mm was machined into disks with diameters of ~

10 mm by electric discharge machining (EDM). The Mg alloy was received as an extruded bar with a diameter of 10 mm, and this bar was cut into disks with a thickness of ~1.2 mm. These Al and Mg disks having 10 mm diameter were mechanically grinded on both surfaces with maintaining a consistent thickness of 0.80 mm by silicon carbide sandpaper.

For the scale-up disk preparation, a plate of Al and an extruded bar of Mg alloy were prepared in the consistent manner as listed for the 10 mm diameter disks but towards to a final thickness of ~2.5 mm with a diameter of ~25 mm after grinding.

3.2 Materials processing

These Al and Mg disks having 10 mm dimeter were processed with conventional HPT facility under quasi-constrained conditions [89,90] in monotonic

torsional straining [91] at RT at 1.0 rpm. A photograph of the HPT machine at Oregon State University is shown in Fig. 3.2.1.

Figure 3.2.1 A photograph of the HPT facility at OSU

In contrast to general HPT processing involving an arbitrarily selected material, this study applies a unique sample set-up where a set of two Al disks and a Mg disk were processed altogether by stacking them in the order of Al/Mg/Al without any special surface treatment between the separate disks. Thus, the initial total thicknesses of the stacked 10 mm and 25 mm diameter disk sets before processing were ~2.4 mm and ~7.5 mm, respectively. The schematic drawing of the unique sample set-up for the mechanical-bonding HPT process is shown in Fig. 3.2.2 where (a) and (c) shows the two different stacked disk specimens with detail dimensions and (b) is the schematic illustration of the experimental set-up.

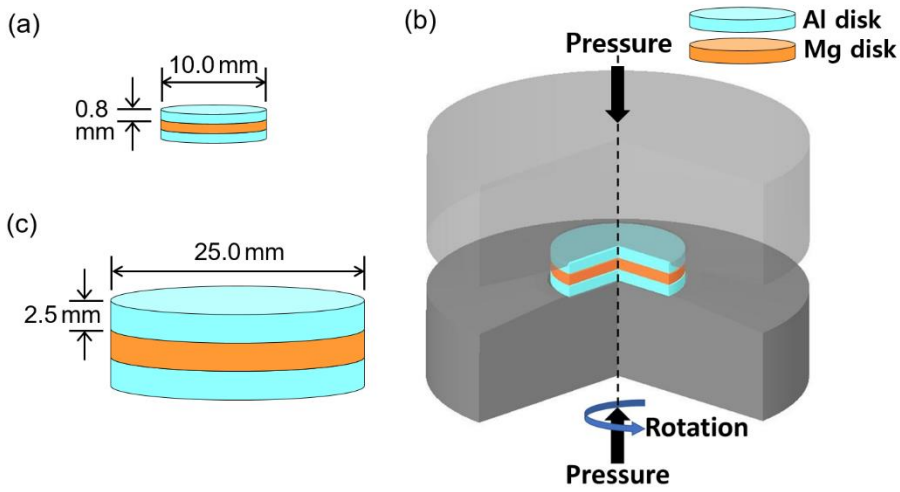

Figure 3.2.2 Schematic drawings of (a) a sample set-up for 10 mm diameter disks, (b) HPT processing for the mechanical bonding, and (c) a sample set-up for 25 mm diameter disks [79]

Two different processing parameters were applied in this study depending on the size of the disks. Series of the standard specimens with 10 mm diameter were processed by HPT under 6.0 GPa at RT for total numbers of revolutions up to 60 turns using a constant rotational speed of 1.0 rpm. On the other hand, the scaled-up specimens having 25 mm diameter were processed through HPT under 1.0 GPa at RT for 10 and 20 turns at a rotational speed of 0.4 rpm. This lower compressive pressure was introduced for the 25 mm diameter disks when the consistent compressive force applied for the 10 mm diameter disks were applied. Moreover, the slower torsional shear rate of 0.4 rpm was selected for the 25 mm disk processing and the shear rate for the large specimen provides an equivalent shear rate for the 10 mm diameter with 1.0 rpm by calculating the shear strain using eq. (3).

3.3 Microstructural analysis

The processed Al-Mg disks with 10 mm and 25 mm diameters were cut

vertically along the diameter into half disks, and a cross-section of each processed disk was mechanically polished to have a mirror-like surface through several various grid size up to 0.05 μm water-based colloidal silica suspension. A series of optical microscope images were taken by an optical microscope, Mitutoyo HM-200, over the polished cross-sectional surfaces after chemically etched with Keller's etchant.

Detailed microstructural analysis was performed using transmission electron microscopy (TEM), JEOL JEOM-2100F, at the edges and centers of the processed disks by HPT. The TEM specimens were prepared by a focused ion beam (FIB), FEI Quanta 3D FEG, where the specimens were taken from the disk edges at $r \approx 4.0$ mm and the disk centers at $r \approx 0$ mm for 10 mm diameter disks and at the disk edges at $r \approx 10.0$ mm for 25 mm diameter disks. In addition, a compositional analysis was conducted using energy dispersive spectroscopy (EDS) in a scanning TEM (STEM) mode.

A series of X-ray diffraction (XRD) analyses were performed using a Rigaku Ultima III for applying the entire disk surfaces to acquire overall structural information of the materials and using a Bruker D8-Discover with a conical shape slit for conducting micro XRD (μXRD) analysis by scanning the small diffracted area of 1.0 mm^2 for obtaining local structural information in areas of interest. Both XRD facilities use Cu Kα radiation at a scanning speed and a step interval of 1° min^{-1} and 0.01°, respectively, and only μXRD analysis for the 25 mm disk after 20 HPT turns was performed under 2° min^{-1} scanning speed and 0.03° step interval due to an instrumental limitation. Further analysis using the XRD profiles was conducted through XRD data analysis software based on Rietveld analysis, Materials Analysis Using Diffraction (MAUD) [92] for identifying and quantifying the phase fractions and changes in the crystal structure, lattice parameter, micro-strain and crystallite size.

3.4 Mechanical properties

Vickers microhardness measurements were conducted to construct hardness profiles along the diameter on the mid-section of each disk sample and color-coded

hardness contour maps on the polished vertical cross-sectional surfaces of the semi-circle disks after processing. The Vickers microhardness values, Hv, were recorded using a Mitutoyo HM-200 with an applied load of 50 gf and a dwell time of 10 s. For the hardness line profile, the hardness measurements were conducted on the near mid-sectional planes of the disk with applying measurement locations as multiple lines pattern by intervals of 0.15 mm. Constructing the hardness maps, the hardness measurements were conducted on the cross-section of the disks with applying measurement locations as a grid pattern by intervals of 0.15 mm.

4. Results

4.1 Formation of metal matrix nanocomposite (MMNC)

4.1.1 Overview of microstructure in an Al-Mg alloy system

Figure 4.1.1 shows the overview taken by an optical microscope of the vertical cross-sections of, from the top, the Al-Mg disks after 1, 5, 10 and 20 turns by HPT [74,76,77,93] and after 20 turns by HPT followed by PDA at 573 K for 1 hour [77,93]. The bright region denotes the Al-rich phase and the dark region denotes the Mg-rich phase after the chemical etching in the micrographs. There was an expected microstructure for the disk after 1 turn showing a multi-layered structure with well-bonded Al and Mg disks without any visible segregation or void at the interfaces of the Al-Mg layers across the disk diameter. It should be noted that the Mg phase is necked and fragmented into islands and these Mg layers tend to become thinner at the disk edge region.

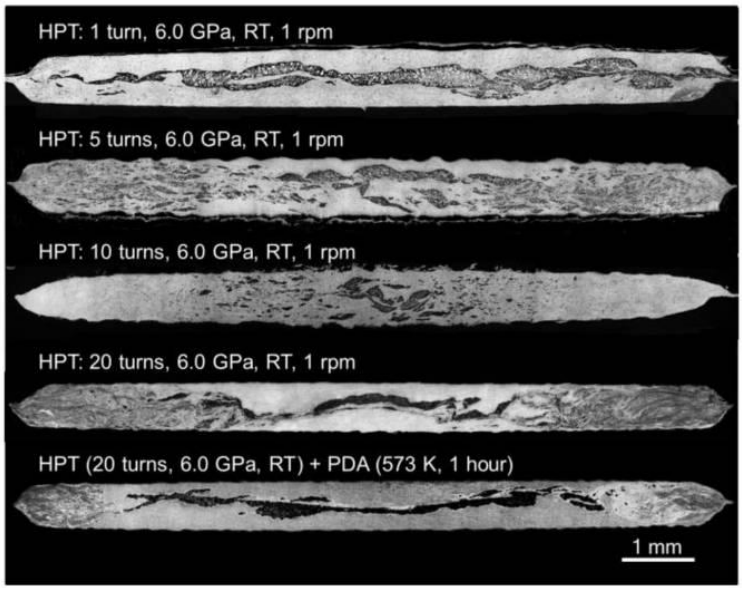

Figure 4.1.1 The optical micrographs on cross-sectional planes of the Al–Mg system after HPT under 6.0 GPa at RT for, from the top, 1, 5, 10, 20 turns and for 20 HPT turns followed by PDA [93]

The HPT-processed disks after 5, 10 and 20 turns demonstrated a unique microstructure with two different microstructural features depend on the radial distance from the centers of the disks. First, the multi-layered microstructure remained in the central regions consistent after 1 turn through 20 turns, but the Mg layers tend to be thinner and fragmented as the number of HPT turns increases. In addition, the multi-layered structure exists at r <2.5 mm of the disk after 5 turns and it becomes narrower to the area with r <1.0 mm after 10 and 20 turns. Second, there is a unique feature at the peripheral regions of the HPT-processed disks up to 20 turns. The disk edge at r >2.5 mm after 5 HPT turns demonstrated homogeneously distributed fine Mg phases with thicknesses of ~200 μm. The peripheral region shows a disappearance of the visible Mg phase optically after 10 and 20 HPT turns and holds the clear flow patterns by torsional straining which is especially apparent after 20 turns. Moreover, the peripheral region without any visible Mg-rich phase is extended to r >2.5 mm after 20 turns while 10 turns showed such severe phase mixing at r >3.0 mm.

A similar single phase-like microstructure was observed after 20 turns followed by PDA, but the area showing severe mixture of phases without a Mg phase was reduced at r >4.0 mm. According to the HPT principles [50,94,95], the peripheral regions having a single phase-like microstructure have an estimated equivalent von Mises strain of >230 and the outer region having a finely distributed Mg phase has the von Mises strain less than 200. It indicates that the hybrid Al-Mg systems after 10, 20 HPT turns and 20 turns followed by PDA have a gradient-type heterostructure along the disk diameter.

4.1.2 Microstructural characterization of an Al-based MMNC

Detailed microstructural and compositional analyses were performed by TEM and XRD at the periphery of the disks after 5, 10 and 20 HPT turns and 20 HPT turns followed by PDA as shown in Figs 4.1.2, 4.1.3, 4.1.4 and 4.1.5, respectively [74,76,77]. Representative TEM bright field image are shown in Fig. 4.1.2(a) and (b) for the disk edge after 5 turns.

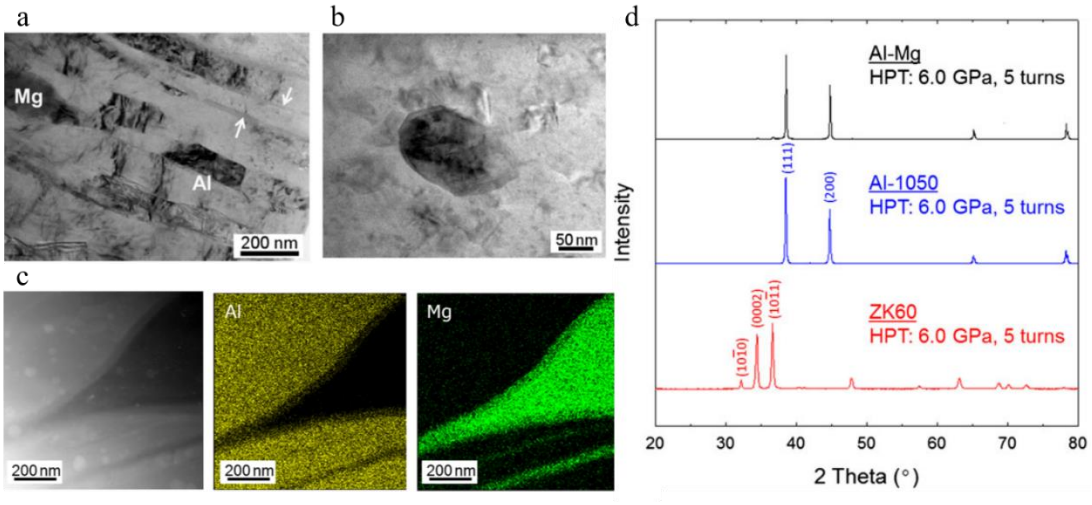

Figure 4.1.2 Representative TEM bright-field images showing (a) a layered microstructure consisting of the Al matrix region with one visible Mg phase, (b) a representative ultrafine grain in the Al matrix and (c) a dark-field image and the corresponding compositional maps of Al and Mg taken at the disk edge after HPT for 5 turns [74] and (d) XRD profiles showing, in ascending order, ZK60A, Al-1050 and the Al–Mg disks after HPT for 5 turns under 6.0 GPa [76]

Firstly, the true nano-scale microstructure was achieved at the disk edge after 5 turns consisting of two representative microstructures, 1) layered microstructures with thickness of ~90-120 nm with well-bonded Al-Mg interfaces without any visible voids and 2) equiaxed microstructures having an average grain size, *d*, of ~190 nm. In addition, several thin layers exist in the layered microstructure with an average thickness of ~20 nm, where these are indicated by white arrows shown in Fig. 4.1.2(a). Further examination through EDS mapping in STEM mode was conducted at the region involving the Al-Mg interface and nano layers as shown in Fig. 4.1.2(c) for a dark field image and corresponding compositional maps for Al and Mg. The compositional analysis through STEM revealed that both thin layers and the Al-Mg interface are composed of both Al and Mg atoms. Further compositional analysis confirmed the thin layers as a β-Al_3Mg_2 intermetallic compound which can be a great source for reinforcing the nanostructured Al matrix towards increasing the hardness and strength at the disk edge of the Al-Mg system [74]. It should be noted that the β-

Al_3Mg_2 was found in a limited area within the Al matrix at the disk edge and these exist only as thin layers.

XRD analysis was conducted at the edge of the Al-Mg disk after 5 turns to provide supporting structural information and a corresponding XRD profile is shown in Fig. 4.1.2(d). For comparison purposes, the XRD profiles for the base materials of ZK60A and Al-1050 after 5 HPT turns are also shown in the plot. It should be noted that all XRD analyses for the Al-Mg disks in this study were performed at the mid-sectional surface of the disks after carefully removing the central regions at r <1.5 mm containing large Mg-rich phases. However, it is difficult to eliminate all existing Mg-rich phase at the disk center and therefore a remaining Mg phase was detected in the XRD analysis.

The XRD profile after 5 turns revealed a very strong *f.c.c.* Al peaks and weak peaks of *h.c.p.* Mg peaks on the (0002) basal plane and $(10\bar{1}1)$ pyramidal plane. In addition to the overall XRD profile analysis, a close inspection on limited 2 theta range from 30° to 60° revealed the existence of a β-Al_3Mg_2 intermetallic compound by relative peak intensity analysis [76]. However, further analysis by MAUD failed to observe the presence of the intermetallic phase. These results support the limited formation of a β-Al_3Mg_2 intermetallic compound at the Al-Mg disk edge after 5 turns, but a fraction of the β-Al_3Mg_2 is less than a detection limit by XRD of 5 vol.%.

An additional evaluation was conducted to estimate the Mg solubility in the Al matrix at the disk edge after 5 HPT turns based on the obtained XRD profile. First, the MAUD computation based on the Rietveld analysis provides a mean lattice parameter of Al of a = 4.0537 Å at the peripheral region of the disk after 5 turns. Based on Vegard's law [96,97] and an experimental study on the lattice expansion by Mg solute in the Al [98], the following equation was established to estimate the Mg solubility, X_{Mg}, in the Al matrix applying the lattice parameter of pure Al, a_0 = 4.0490 Å [99].

$$X_{\mathrm{Mg}} = 9.045\left(\frac{a - a_0}{a_0}\right) \pm 0.003 \qquad (5)$$

Thus, eq. (5) provides an estimated Mg solubility in the Al matrix of 0.5 at.% ± 0.3 and it is reasonable to conclude that the estimated solubility represents an average concentration of Mg in the Al matrix at r >1.5 mm after 5 turns by considering the diffraction area by XRD analysis. This value is more than ten times of Mg concentration in the Al-1050 base material, however it is lower than the maximum solubility of Mg of ~1.6 at.% in Al at RT [100] and there is no evidence of the supersaturated solid solution (SSSS) formation. Therefore, processing of Al and Mg alloy altogether by HPT for 5 turns demonstrated a formation of an Al-based metal matrix nanocomposite (MMNC) containing an intermetallic compound of β-Al_3Mg_2.

Figure 4.1.3(a) shows a representative TEM bright field image at the edge of the Al-Mg system after 10 turns [74]. It shows much finer microstructure than after 5 turns shown in Fig. 4.1.2(a) and (b). No proof of the presence of a Mg-rich phase was observed within the specimen prepared by FIB and there are equiaxed grains with an average size of ~90 nm.

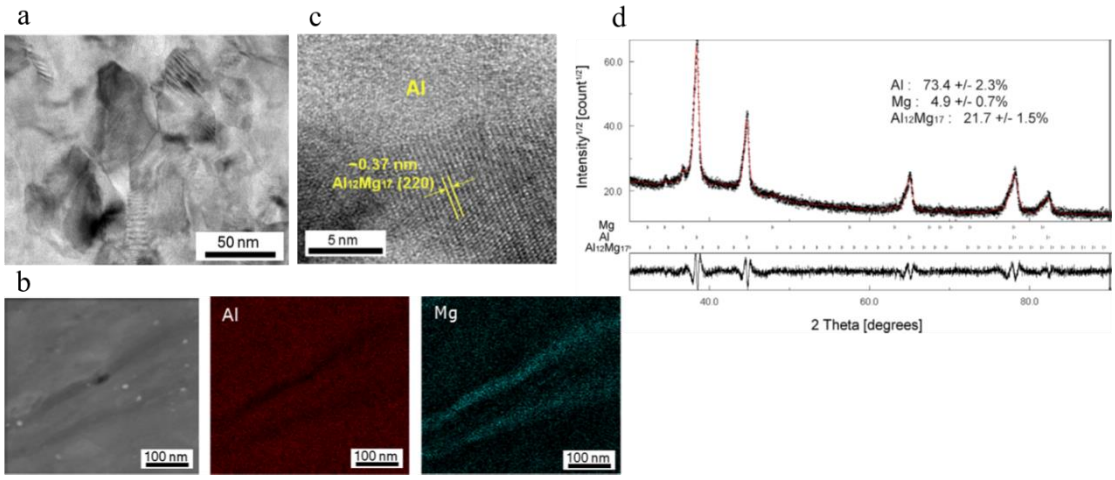

Figure 4.1.3 (a) A representative bright-field image, (b) a dark-field image and the corresponding compositional maps of Al and Mg, (c) a high resolution TEM image taken in the Al matrix and (d) XRD profile in black and the simulated line profile in red at the edge of the Al-Mg system after HPT for 10 turns [74]

Also, a similar microstructure was confirmed by EDS in STEM mode shown in Fig. 4.1.3(b). It demonstrates a formation of a nanolayered structure with a thickness of ~30 nm in the Al matrix. Moreover, the EDS mapping result shows that a relatively large content of Mg is dissolved into the Al matrix at the disk edge after 10 turns resulting in a difficulty to clarify the Al-Mg interface boundaries which is in contrast with the disk edge after 5 turns.

Compositional analysis by EDS point scanning confirmed the presence of β-Al_3Mg_2 intermetallic compound as nano-scale thin layers in the Al matrix as well as the Mg dissolution of ~9.0 at.% in the Al matrix [74]. Furthermore, a high-resolution TEM (HR-TEM) image taken at the nanostructured Al matrix shown in Fig. 4.1.3(c) demonstrates the presence of γ-$Al_{12}Mg_{17}$ intermetallic compound having an atomic spacing of ~0.37 nm at a (220) plane that is a larger interatomic spacing than any planes in the Al phase. Figure 4.1.3(d) shows the XRD profile with a black line and a fitted line through MAUD with a red color and the estimated phase fractions. The estimation provides 73.4 ± 2.3 of Al, 4.9 ± 0.7 of Mg and 21.7 ± 1.5 of a γ-$Al_{12}Mg_{17}$ intermetallic compound in wt.%. The presence of β-Al_3Mg_2 intermetallic compound which was confirmed by compositional analysis was not observed by XRD and MAUD analyses. It implies that the concentration of β-Al_3Mg_2 is less than the detectable limit by XRD at the edge of the Al-Mg system after 10 turns.

Furthermore, using eq. (5) and the estimated lattice parameter of a = 4.0628 Å for the Al-Mg disk edge after 10 HPT turns, the Mg solubility in Al matrix was calculated as 3.1 at.% and it is much higher than the maximum solubility limit in the Al matrix at RT. These results provide a direct proof of the formation of MMNC with nanocrystalline Al SSSS and two different intermetallic compounds. However, there is no supporting evidence of the preferred location in formation of β-Al_3Mg_2.

A set of the results through TEM and XRD are shown in Fig. 4.1.4 for the Al-Mg system after 20 turns at the peripheral regions [77]. Figure 4.1.4(a) and (b) are representative TEM bright-field images, (c) a corresponding selected area diffraction (SAED) pattern from the region in (b), (d) a dark-field image in STEM mode from the region in (a) and the corresponding compositional maps for Al and Mg, and (e) a selected 2 theta range X-ray profile taken at the disk edge of the Al-Mg system after 20 turns.

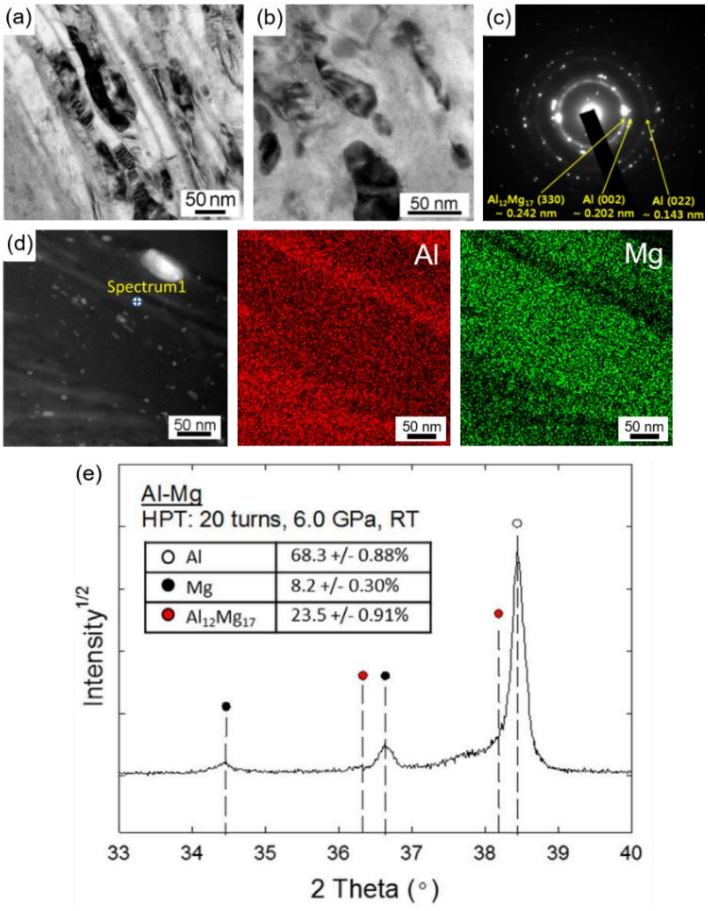

Figure 4.1.4 (a) and (b) Representative TEM bright-field images, (c) the corresponding diffraction ring patters taken at the equiaxed microstructural region, (d) a dark-field image and the corresponding compositional maps of Al and Mg, and (e) XRD profile taken at the disk edge of the Al-Mg system after HPT for 20 turns [77]

The TEM micrographs taken at the disk edge after 20 turns revealed the existence of two representative microstructures consist of layered and equiaxed grain formations. An average thickness of the layered structure is ~20 nm containing numerous dislocations which penetrate the layers in a vertical direction and an average spatial grain size is ~60 nm in the equiaxed microstructure.

Figure 4.1.4(c) provides a direct proof of the formation of a γ-$Al_{12}Mg_{17}$ phase by spot distributions in the SAED pattern. A compositional analysis at the layered microstructure as shown in Fig. 4.1.4(d) revealed two important findings. First, no Mg-rich phase was observed at the disk edge after 20 turns, thereby implying the complete dissolution of Mg in the nanocrystalline Al-rich matrix. Second, as displayed in Fig. 4.1.4(d), all the measured area consists of both Al and Mg atoms, thereby indicating no clear phase interfaces at the disk edge of the Al-Mg system. A point element analysis was conducted at a marked point displayed as Spectrum 1 in Fig. 4.1.4(d). The point was randomly selected within the thin layers of an thickness of ~20 nm and the concentration of each atom is ~57.55 at.% of Al and ~41.84 at.% of Mg, thereby demonstrating the formation of β-Al_3Mg_2 as thin layers in the Al matrix.

Figure 4.1.4(e) shows the XRD profile with a table showing compositional data taken through MAUD for the Al-Mg disk edge after 20 HPT turns. Thus, the estimated phase fractions are 68.3 ± 0.9 of Al, 8.2 ± 0.3 of Mg and 23.5 ± 0.9 of γ-$Al_{12}Mg_{17}$ phases in wt.%. The Mg-rich phase were detected from the multi-layered structure at the central region which is inevitable to eliminate by the sample preparation. Moreover, it was unable to detect the β-Al_3Mg_2 even though the presence of the β-Al_3Mg_2 nano-layers were confirmed in STEM. It suggests the fraction of β-Al_3Mg_2 phase at the disk edge after 20 turns is less than the detectable limit by XRD. Nevertheless, there was an increase in the concentration of the γ-$Al_{12}Mg_{17}$ intermetallic compound at the disk edge after 20 turns than 10 turns. In addition, using eq. (5) and the estimated lattice parameter for the disk edge of a = 4.0643 Å, the calculated Mg solubility in Al matrix was ~3.43 at.% at the disk edge of the Al-Mg system after 20 turns, thereby demonstrating the formation of the Al SSSS. It is

reasonable to conclude that the XRD analysis shows an excellent agreement with microstructural and chemical analyses conducted by TEM where the peripheral region of the Al-Mg system for 20 turns forms MMNC containing the two intermetallic compounds of β-Al_3Mg_2 and γ-$Al_{12}Mg_{17}$ within Al SSSS.

A series of consistent microstructural and compositional analysis was conducted at the edge of the Al-Mg system for 20 turns followed by PDA at 573 K for 1 h. Figure 4.1.5(a) is a representative TEM bright-field image, (b) a corresponding HR-TEM image from the selected area in (a), (c) a dark-field image in STEM mode from the region in (a) and the corresponding compositional maps of (d) Al and (e) Mg, and (f) the X-ray profile taken at the disk edge after 20 turns followed by PDA [77].

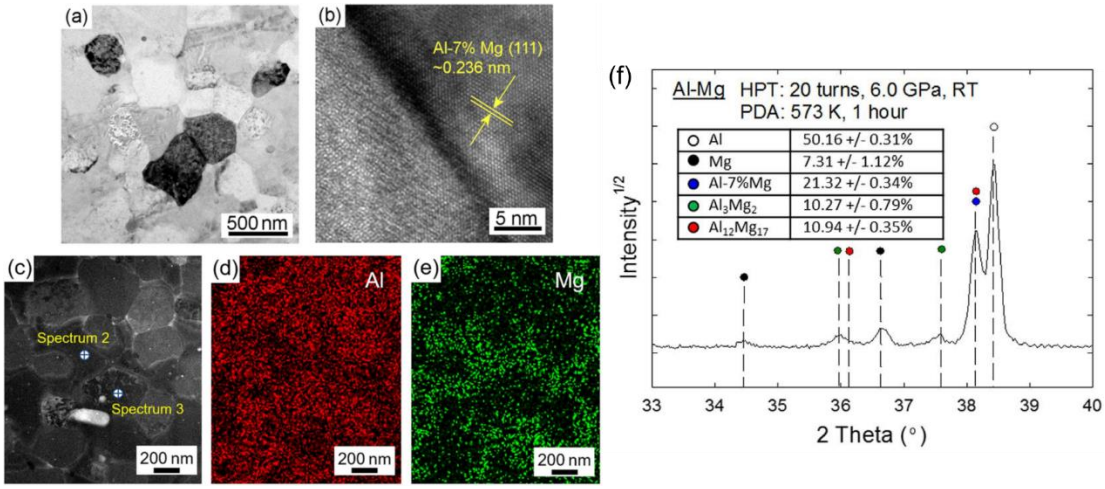

Figure 4.1.5 (a) A representative TEM bright-field image, (b) a high-resolution TEM image, (c) a dark-field image and the corresponding compositional maps of (d) Al and (e) Mg, and (f) XRD profile taken at the disk edge of the Al-Mg system after HPT for 20 turns followed by PDA [77]

It is apparent that the Al-Mg system after 20 turns followed by PDA has homogeneous microstructure with an average equiaxed grain size of ~380 nm, thereby confirming grain growth by PDA after HPT for 20 turns. Moreover, a grain having an atomic spacing of ~0.236 nm was observed in HR-TEM as shown in Fig. 4.1.5(b) and anticipating a lattice expansion due to substitutional Mg dissolution the measured

lattice parameter corresponds to an interplanar spacing of (111) plane for an Al-7% Mg solid solution alloy [98].

The Al and Mg element maps as shown in Fig. 4.1.5(d) and (e) display a clear evidence that Mg is dissolved in all grains with different distributions in adjacent grains. A point element analysis at Spectrum 2 and 3 revealed the specific element fractions of ~59.02 at.% of Al and ~40.04 at.% of Mg, thus implying a β-Al_3Mg_2 intermetallic compound, and ~91.42 at.% of Al and ~8.58 at.% of Mg, thus denoting an Al-7% Mg solid solution, respectively. It should be noted that the spectrum 3 has a higher Mg concentration than 7% and it is caused by the general trends showing a higher Mg concentration in Al solid solution than the nominal composition of Al-Mg alloy [101,102]. However, there was no evidence of a γ-$Al_{12}Mg_{17}$ phase in the measured region while the phase was observed at the disk edge after HPT prior to PDA. On the contrary, XRD analysis followed by the MAUD computation provided element concentrations of 50.2 ± 0.3 of Al, 7.3 ± 2.2 of Mg, 21.3 ± 0.3 of Al-7% Mg, 10.3 ± 0.8 of β-Al_3Mg_2 and 10.9 ± 0.4 of γ-$Al_{12}Mg_{17}$ in wt.%. The Mg content detected by XRD analysis is due to the Mg-rich phase existing close to the disk center. Nevertheless, the HPT-induced Al-Mg disk after PDA demonstrated a new type of MMNC involving two intermetallic compounds with an Al-7% Mg solid solution phase which is in contrast with the Al-Mg disk immediately after 20 turns containing significant concentration of γ-$Al_{12}Mg_{17}$ in the MMNC at the disk edge.

4.1.3 Exceptional hardness in the Al-based MMNC

To evaluate the mechanical properties of the Al-Mg system after different numbers of HPT turns and additional PDA, the Vickers microhardness values were measured on the vertical cross-sections of the Al-Mg system for 1-20 turns and 20 turns followed by PDA [74,77]. The recorded hardness values were displayed as color-coded contour maps that were overlapped with the corresponding optical microscope images as shown in Fig. 4.1.6(a) [93]. For visualizing the hardness evolution with increasing numbers of HPT turns, the average hardness profiles were

constructed by taking the hardness values along the disk diameter on the mid-thickness of the vertical cross-sections of the Al-Mg system and the result is shown in Fig. 4.1.6(b). In the hardness profile, the dotted lines in red and blue indicate a saturated hardness value of Hv ≈ 65 [51] and ≈ 110 [52] for Al-1050 and ZK60A alloys after 5 HPT turns for references.

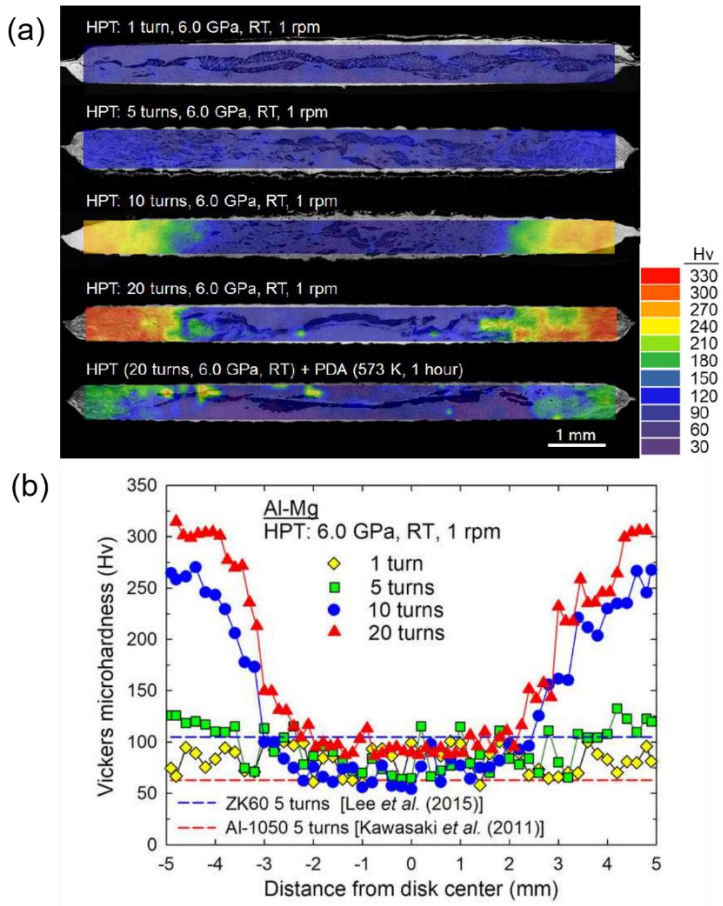

Figure 4.1.6 (a) Color-coded hardness contour maps taken at the vertical cross-section and (b) hardness variation along the disk diameter of the Al-Mg system after HPT for 1, 5, 10 and 20 turns and after HPT for 20 turns followed by PDA [93]

The hardness map for the Al-Mg system after 1 turn shows microhardness values of Hv ≈ 60-70 all over the disk cross-section where the values are similar to the saturated hardness of Hv ≈ 65 for the Al-1050 alloy. Moreover, this hardness value remains reasonably consistent at the central regions at r <2.5–3.0 mm of the Al-Mg

system up to 20 turns because there was no significant microstructural evolution in the central regions of the Al-Mg system through 20 turns. On the contrary, the disk peripheral regions tend to introduce a significant increase in hardness after 5 or higher turns. The hardness value of Hv ≈ 130 was recorded at the disk edge after 5 turns where the finely distributed Mg phase exists. Furthermore, the recorded hardness after 10 turns is drastically increased from Hv ≈ 70 at r <2.0 mm to Hv ≈ 110 at r ≈ 3.0 mm and ultimately increased to Hv ≈ 270 at r >4.0 mm. After 20 HPT turns, an exceptional hardness of Hv ≈ 330 was achieved at r >3.5 mm, while the hardness remains as Hv ≈ 70 at the central region at r <2.5 mm. On the other hand, after 20 HPT turns and PDA, the hardness decreased to ~220 at the outer region at r >4 mm and a decrease in the hardness of central regions to Hv ≈ 30 at r <3.0 mm.

It is defined that the accelerated diffusivity of Mg atoms in the Al matrix under high compressive pressure during HPT is the main reason for the diffusion bonding of Al and Mg at room temperature, ultimately leading to the formation of intermetallic compounds through HPT [74,76]. Several studies reported the experimental evidence for accelerated atomic diffusion in the BNM processed through ECAP [103,104] and HPT [74,105]. There may be several factors to enhance the diffusivity in materials through the application of SPD. The factors include a high hydraulic pressure with a limited temperature increase during processing [74] and a concurrently applied torsional stress to the material under torsion during HPT processing [105], and the generation of numerous lattice defects in the nanostructure after SPD [104]. In practice, an earlier review describes the significant increase in the vacancy concentration during SPD processing which attributed to the fast-atomic mobility of the processed materials [16].

4.2 Enhancement of solid-state reaction by parameter control

4.2.1 Effect of a torsional strain on mechanical bonding

Figure 4.2.1(a) shows the overall cross-sectional microstructures taken by an optical microscope and the corresponding hardness distributions displayed as the

color-coded contour maps for the Al-Mg system after HPT for 40 (upper) and 60 (lower) turns [78]. For the micrographs, the darker regions denote Mg-rich phases and the brighter regions denote Al-rich phases, and both hardness contour maps have a consistent scale color key for comparison purposes. It is reasonable to compare the microstructure in Fig. 4.2.1 with Fig. 4.1.1 for the Al-Mg system up to 20 turns by HPT to evaluate the microstructure evolution with increasing numbers of turns.

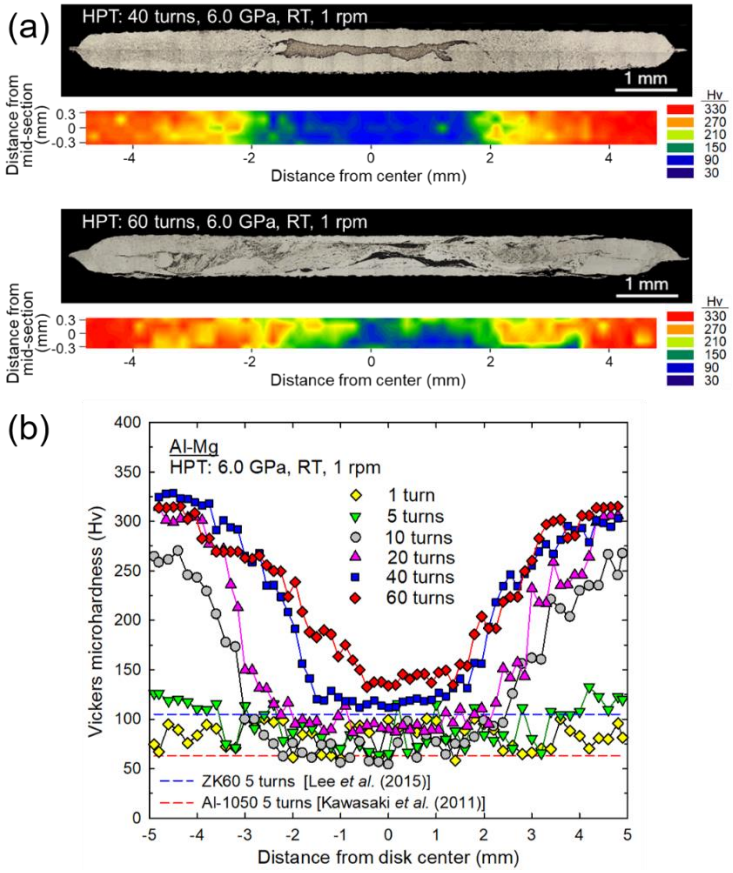

Figure 4.2.1 (a) Overview of the cross-sections and the corresponding hardness color contour maps for the Al-Mg system after HPT for 40 (upper) and 60 turns (lower), (b) hardness variation along the disk diameters at the mid-thickness on the cross-sections of the Al-Mg disks after HPT for up to 60 turns [78]

It is apparent that increasing numbers of HPT turns through 40 and 60 turns result in the extended peripheral regions showing a single phase-like microstructure.

There is an interesting feature in microstructure and hardness at the disk edge after 40 and 60 turns where a significantly high hardness of Hv ≈ 330 at the expanded regions at r >~2 mm. Moreover, there was no significant increase in a maximum hardness at the peripheral regions after 20 turns towards 60 turns for the Al-Mg system. Therefore, it is reasonable to conclude that the maximum hardness value of Hv ≈ 330 is in a reasonably saturated condition for the Al-Mg system and increasing HPT turns results in the wider peripheral region involving the single phase-like microstructure, ultimately leading to a potential to show a saturated microstructure throughout the disk.

It is reasonable to place all the hardness profiles along the disk diameter in a single figure to evaluate the evolution in hardness with increasing torsional turns from 1 to 60 turns for the Al-Mg system processed by the mechanical bonding and the plot is shown in Fig. 4.2.1(b) [78]. These series of the hardness values represent the average hardness taken at the mid-sections of the Al-Mg system and the dotted lines at Hv ≈ 65 [51] and ≈ 110 [52] are the saturated hardness of the Al-1050 and ZK60A alloys after 5 turns, respectively. There is an apparent shift of the disk center in terms of the radial symmetry of the hardness variation in HPT-processed materials [53] and it is caused by the inevitable misalignment of the upper and lower anvils that is especially obvious at higher numbers of HPT turns. However, an earlier study demonstrated the fact that the misalignment of the anvils does not influence the high hardness values at the disk edge except the shifting of locations with lower hardness indicating the disk centers [106].

It is apparent that relatively high hardness was widened at the disk edge at r ≈ 2.0 mm and the maximum hardness of ~330 was observed at r >4.0 mm after both 40 and 60 turns, while the low hardness of Hv ≈ 120 and 150 at the disk centers having a layered microstructure remained at r <1.5 mm and <0.7 mm for 40 and 60 turns, respectively. Thus, the results demonstrate that the increase in HPT turns leads the shrinkage of the area showing the layered microstructure at the disk centers.

For detailed structural analysis, μXRD analysis was performed at the disk edges of the Al-Mg system after HPT for 40 and 60 turns and the XRD profiles are shown in Fig. 4.2.2 [78]. It should be noted that μXRD analysis enables to conduct a structural evaluation by XRD at a limited region of interest and thus the examinations were focused at the disk edges of the Al-Mg disks after the mechanical bonding for 40 and 60 turns.

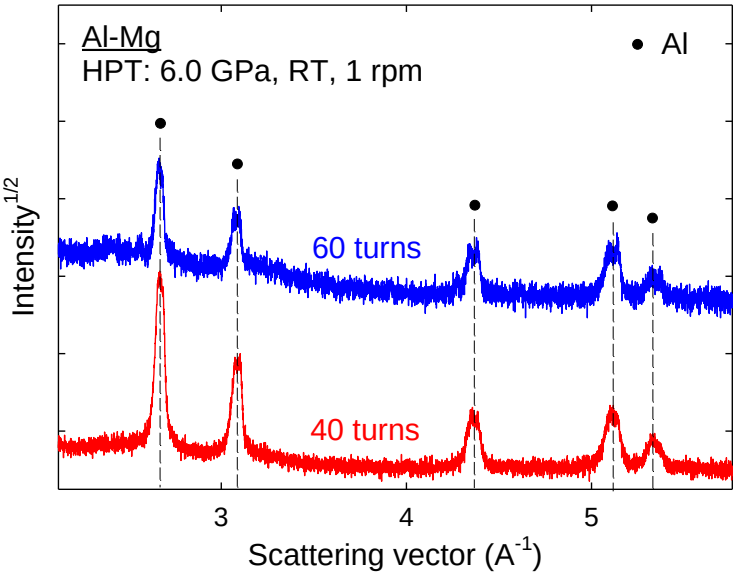

Figure. 4.2.2 XRD line profiles taken at the disk edge of the Al-Mg disks after HPT for 40 (lower) and 60 turns (upper) obtained by μXRD [78]

It is apparent that there are five strong peaks such as 111, 200, 220, 311 and 222 which are representative for Al in *f.c.c.* in the XRD profiles, thereby implying the presence of an Al-rich phase without Mg-rich or any intermetallic phases at the peripheral regions after 40 and 60 turns. The result was confirmed by the compositional analysis by MAUD using the XRD data providing the phase concentrations of Mg, β-Al_3Mg_2 and γ-$Al_{12}Mg_{17}$, of less than 0.01 wt.%. Thus, the high numbers of HPT turns to 40 and 60 demonstrated the mechanically-bonded Al-Mg system having solely Al phase without any second phase which is in contrast to

the presence of γ-$Al_{12}Mg_{17}$ of over 20 wt.% at the disk edge of the Al-Mg system after 10 and 20 turns as shown in Figs 4.1.3 and 4.1.4, respectively.

To estimate the Mg solubility in the Al matrix, the lattice parameters of the Al phase were calculated by the peak fitting using the XRD data for the Al-Mg disk edges after 40 and 60 HPT turns. Moreover, the Mg solubility were calculated based on the eq. (5), and a coherent crystallite size and micro-strain were estimated through the Williams-Hall method using the XRD profiles [107,108]. These results are summarized in Table 1 for the disk edges of the Al-Mg system after HPT for 40 and 60 turns [78].

Table 1 Summary of estimated lattice parameter of Al, the Mg concentration in the Al matrix, the coherent crystallite size, and the micro-strain for the disk edges of the Al-Mg system with 10 mm diameter after HPT for 40 and 60 turns. [78]

	HPT: 40 turns	HPT: 60 turns
Lattice parameter of Al (Å)	4.0773	4.0796
Mg concentration in the Al matrix (at.%)	6.62 ± 0.3	7.14 ± 0.3
Coherent Crystallite size (nm)	~41	~28
Micro-strain	0.0143	0.0113

The peaks tend to shift to the lower scattering angle, Q, and become broadened with increasing numbers of HPT turns. It indicates an increase in the lattice parameter of Al leading to an increase in the Mg concentration and a decrease in coherent crystallite size with a reasonably consistent micro-strain at the disk edges. The Mg concentration increased to 6.6 and 7.1 at.% in the Al matrix at the disk edges after 40 and 60 turns, respectively, and it is in contrast with a Mg content of 3.43 at.% at the disk edge involving an MMNC after 20 turns. These results suggest the dissolution of the intermetallic compounds which were existed at the disk edge after 20 HPT turns into the Al matrix after 40 HPT turns. The coherent crystallite size was estimated as ~40 nm and ~30 nm at the disk edge after 40 and 60 HPT turns, respectively. The coherent crystallite size is expected to be slightly smaller than the actual grain size in

the polycrystalline materials, especially it is apparent in the SPD-processed materials where many sub-grains exist within the materials. Nevertheless, it is apparent that the significant grain refinement happened in the Al matrix at the disk edge through 60 turns by HPT. Nevertheless, further detailed microstructural analysis is required to investigate the evolution of the microstructure of the Al-Mg system after high numbers of HPT turns.

4.2.2 Size effect on a mechanical bonding

Figure 4.2.3(a) shows the overview of the microstructure at the vertical cross-sections of the Al-Mg system with 25 mm diameter captured by an optical microscope and the corresponding hardness distributions displayed as the color-coded contour maps for 10 turns (upper) and 20 turns (lower) processed under 1.0 GPa at 0.4 rpm with the same hardness scale used in Fig. 4.2.1 for the 10 mm diameter disks [79]. The hardness distributions with the error bars along the disk diameter are shown in Fig. 4.2.3(b) for these two HPT-processed Al-Mg system having 25 mm diameter.

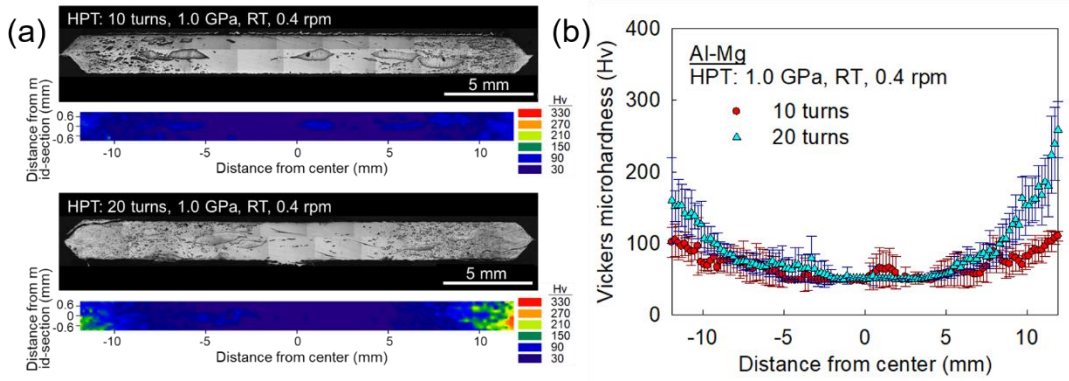

Figure 4.2.3 (a) Cross-sectional micrographs and the corresponding hardness color contour maps for the Al-Mg disks with 25 mm diameter after HPT for 10 turns (upper) and 20 turns (lower) under 1.0 GPa at 0.4 rpm, and (b) the hardness valuation with the standard error along the disk diameter for these two mechanically-bonded Al-Mg disks [79]

In the optical microscope images, a brighter region denotes an Al-rich phase and a darker region denotes a Mg-rich phase. There are large fragmented Mg-rich phases at $r \leq 7.0$ mm that are mainly located near mid-thickness of the disk and finer Mg-rich phases are distributed homogeneously at the overall vertical cross-section at $r \geq 7.0$ mm after 10 turns by HPT.

On the contrary, a microstructure of the Al-Mg system having 25 mm diameter shows three representative sections after 20 HPT turns; The large fragments of a Mg-rich phase at $r \leq 5.0$ mm, finer Mg-rich phases at 5.0 mm < r <10.0 mm and a single phase-like microstructure with torsional flow patterns at r >10.0 mm. In terms of hardness evolution, a typical hardness evolution was observed in the Al-Mg system having 25 mm diameter where low hardness exists at the disk centers and the hardness increases toward the disk edges. The trend is more apparent when increasing numbers of HPT turns from 10 to 20 turns for the 25 mm diameter disks.

Figure 4.2.3(b) demonstrates that the central region at $r \leq 7.0$ mm corresponding to the large Al phase shows the Vickers microhardness value of ~50 and the hardness value is gradually increases to Hv ≈ 100-110 towards the disk edge after 10 HPT turns and the hardness at the disk edge is consistent with the reference hardness value of the ZK60A Mg alloy in a saturated condition after 5 HPT turns [52]. The hardness at the central region remains constant as ~50 with increasing numbers of HPT turns up to 20 for the Al-Mg system having 25 mm diameter. The hardness tends to increase at the disk edge, but a limited peripherals region tends to show higher hardness with the highest value of Hv ≈ 250 whereas other peripheral region shows the hardness value of Hv ≈ 200. This asymmetrical hardness distribution is caused by the misalignment of the HPT anvils and it tends to appear at higher numbers of HPT turns.

There is an apparent difference in microstructure at the central regions between the 10 mm and 25 mm diameters disks of the Al-Mg system processed by the mechanical bonding. There are multi-layered microstructures at the disk centers up to 60 turns in the 10 mm diameter disks shown in Figs 4.1.1 and 4.2.1(a) whereas little

fragmented Mg phase exists within the Al matrix in the disk having 25 mm diameter as shown in Fig. 4.2.3(a). A significant loss of sample volumes occurred for processing of the 25 mm diameter disks mainly during the compression process and an early stage of torsional straining under a pre-determined pressure and it may attribute to a significant loss of the Mg phase at the central regions. In practice, a total thickness of the disk with for 25 mm diameter before HPT processing was ~7.5 mm and the final thickness after HPT processing was ~2.4 mm where the excess of materials flow out between a pair of the anvils due to the principles of quasi-constrained HPT [89,90] and the stress concentration may be the highest at the mid-section of the stacked materials.

Figure 4.2.4 shows (a) a representative TEM bright field image, (b) the corresponding SAED pattern and (c) a dark-field image in STEM mode taken at the region in (a) with a corresponding element maps for the Al-Mg disk edge at $r \approx 10$ mm after 20 HPT turns [79].

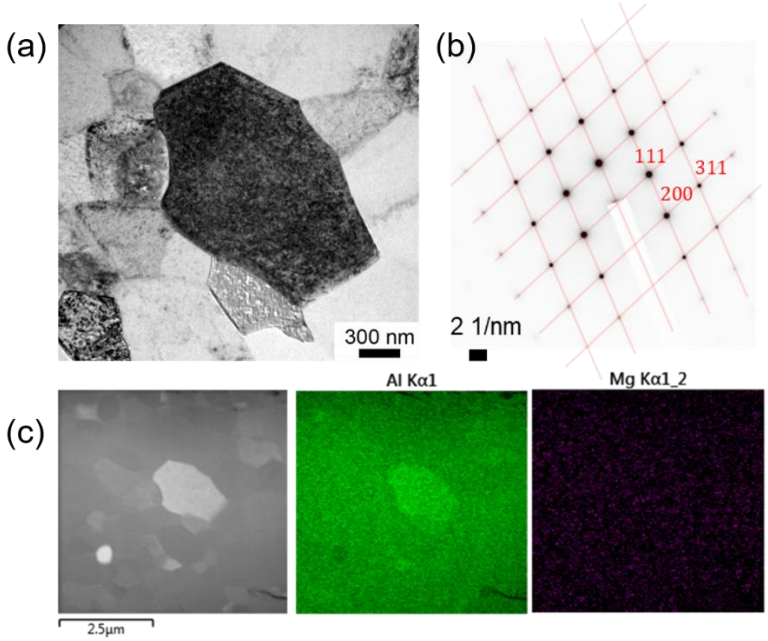

Figure 4.2.4 (a) A representative TEM bright-field image, (b) the corresponding selected area electron diffraction (SAED) pattern and (c) a dark-field image and the

corresponding element mapping taken at the disk edge at r ≈ 10 mm after HPT for 20 turns under 1.0 GPa at 0.4 rpm [79]

There were only equiaxed grains with clear grain boundaries within the FIB-prepared specimen for the material. Specifically, there were several grains with sizes over 500 nm as shown in Fig. 4.2.4(a), while an average grain size was estimated as ~ 380 nm. The SAED pattern shown in Fig. 4.2.4(b) reveals a typical diffraction pattern of an *f.c.c.* structure consisting of 111, 200 and 311 planes, which implies a presence of only Al phase. There is no evidence of second phase, such as *h.c.p.* Mg and any intermetallic phases, in the diffraction pattern taken at different locations within the TEM specimen. The element mapping shown in Fig. 4.2.4(c) provides a supporting evidence that the evaluated microstructure mainly consisted of an Al-rich phase with a dispersion of Mg atoms within the Al in the Al-Mg system with 25 mm diameter after 20 HPT turns. However, these results are obtained at a limited area and unable to represent the microstructure at the entire disk edge of the Al-Mg system with 25 mm diameter after 20 turns.

Further microstructural analysis was conducted by μXRD at a consistent location at the disk edge where the TEM micrograph in Fig. 4.2.4(a) was taken, a mid-radius and near-center for the Al-Mg system having 25 mm diameter after HPT for 10 and 20 turns. The XRD profiles are shown in Fig. 4.2.5(a) and (b) for the disks after 10 and 20 turns, respectively, and the quantitative results based on the MAUD computation were summarized in Table 2 for the measured locations where at least two phases were detected by XRD.

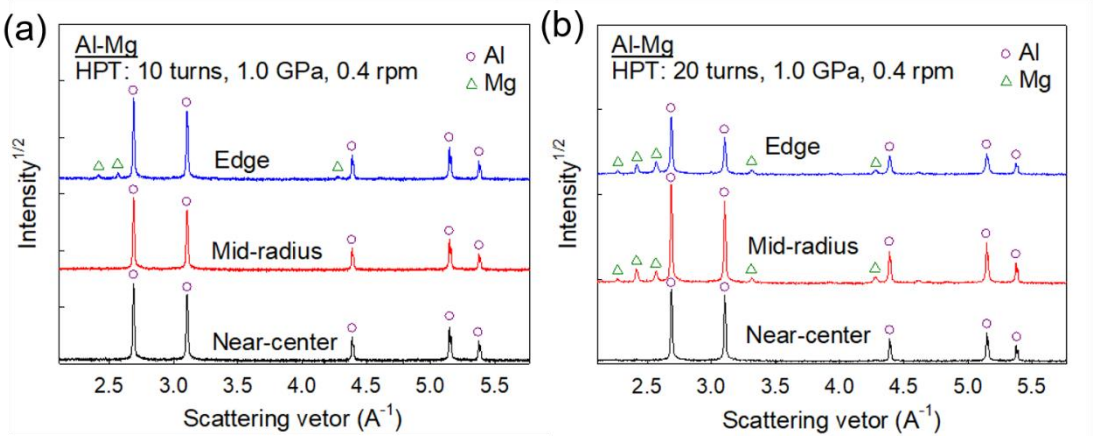

Figure 4.2.5 XRD profiles conducted by μXRD at three different locations of near-center, mid-radius and edge of the Al-Mg disks with 25 mm diameter after HPT for (a) 10 and (b) 20 turns [79]

Table 2 The results on compositional analysis by MAUD based on the XRD patterns shown in Fig. 4.2.5 [79]

25 mm diameter disk	location	Al matrix (wt.%)	Mg matrix (wt.%)
Al-Mg 10 turns	Edge	98.70	1.29 ± 0.01
Al-Mg 20 turns	Edge	88.71	11.29 ± 0.58
Al-Mg 20 turns	Mid-radius	93.38	6.62 ± 0.18

A series of strong diffraction peaks for an *f.c.c.* structure consisting of 111, 200, 220, 311 and 222 reflections appeared for all measured locations along the disk radius for both disks having 25 mm diameter after 10 and 20 HPT turns. the Weak peaks for an *h.c.p.* Mg were observed at the disk edges after 10 and 20 turns and at the mid-radius after 20 turns. Specifically, the disk edge after 10 turns includes ~1.5 wt.% of Mg phase and the disk mid-radius and edge after 20 turns contain ~6.2 wt.% and ~11.3 wt.% of Mg, respectively. It should be noted that the three regions containing Mg phase examined by μXRD were two phase co-existing regions without any dissolution of Mg atoms into the Al-matrix. Moreover, comparing the 10 mm and 20 mm diameter disks, no consistent trend of phase distributions was observed at the

locations where consistent equivalent distances from the disk centers. The lattice parameters of Al were calculated for all locations and these were used for estimating the Mg solubility in the Al matrix using the method described in the section 4.1 and, in addition, the crystallite size and the micro-strain were estimated with an application of the Williamson-Hall method at the near-center, mid-radius and near-edge of the disk with 25 mm diameter and the peripheral regions of the disk with 10 mm diameter.

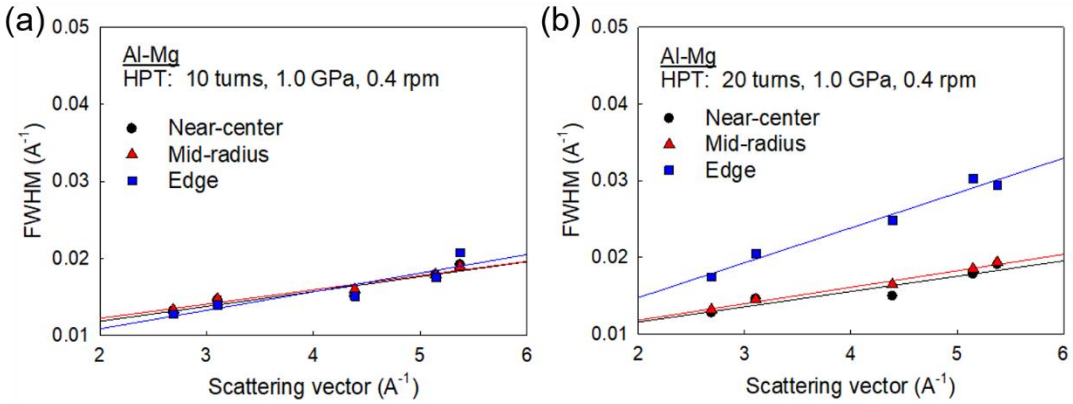

Figure 4.2.6 Conventional Williamson-Hall plots for the Al-Mg system with 25 mm diameter after HPT for (a) 10 and (b) 20 turns under 1.0 GPa at 0.4 rpm [79]

Table 3 Summary of estimated lattice parameter of Al, the Mg concentration in the Al matrix, the micro-strain and the crystallite size for different measurement locations of center, mid-radius and edge of the Al-Mg disks with 25 mm diameter [29]

25 mm diameter disks						
	10 turns			20 turns		
	Near-center	Mid-radius	Edge	Near-center	Mid-radius	Edge
Lattice parameter (Å)	4.0507	4.0514	4.0520	4.0515	4.0520	4.0536
Mg contents (at.%)	0.37	0.53	0.67	0.56	0.68	1.03
Micro strain	0.00795	0.00848	0.00600	0.00750	0.00565	0.00084
Crystallite size (nm)	325.1	339.2	260.2	315.0	292.3	138.1

There are consistent trends of increases in the Al lattice parameters and of increases in equivalent strain calculated by eq. (4) from near-center to edge for the Al-Mg system having 25 mm diameter after HPT for 10 and 20 turns. The calculated Al lattice parameters for the 20 turns disk are consistently larger than the 10 turns disk at all consistent locations due to a higher torsional strain by increasing numbers of HPT turns. Moreover, an increase in the Al lattice parameter is directly correlated with an increase in Mg solubility in the Al matrix for the Al-Mg system with the increasing distances from the disk center and numbers of HPT turns. The Mg solubility at all measurement locations after both 10 and 20 turns are less than the solubility limit of Mg of ~1.6 at.% in Al at RT and thus there is no evidence of an SSSS formation in the Al-Mg disks with 25 mm diameter.

The value of micro-strain reaches the highest at the mid-radius and the lowest at the disk edge for the disks having 25 mm diameter after both 10 and 20 HPT turns. It is generally anticipated to observe the maximum micro-strain at the disk edge where the torsional strain is the highest leading to lattice distortion and higher dissolutions of Mg atoms in the Al matrix. Thus, the lowering of micro-strain at the disk edge may be attributed to a significant loss of the material volumes during the mechanical bonding by HPT processing, thereby demonstrating a stress release. The changes in a crystallite size show a reasonable trend where a decrease in crystallite size with increasing numbers of HPT turns and distance from the disk center. In practice, the crystallite sizes at the disk edges are ~260 nm and ~140 nm after HPT for 10 and 20 turns, respectively. Comparing the results between the two different HPT sample sizes, it is concluded that the edges of the disks with 10 mm diameter demonstrate dramatic changes in microstructure while a torsional speed during HPT is equivalent for all disk edges having both 10 mm and 25 mm.

5. Discussion

5.1 Strengthening mechanisms in MMNCs

The synthesized Al-Mg system demonstrated extraordinary hardness at the peripheral regions after HPT processing up to 60 turns. In practice, the Al-Mg system after HPT up to 20 turns showed the formation of intermetallic-based MMNCs at the disk edges. Specifically, the Al-Mg disks after 5 HPT turns started to increase hardness higher than the upper limit of the base materials and after 10 turns through HPT led to super saturation of Mg in the Al matrix. Accordingly, it is reasonable to investigate the potential strengthening mechanisms for the Al-Mg system up to 10 turns where the study can focus more on the early stage of the formation of intermetallic phases.

Three strengthening mechanisms may be considered for inducing the extraordinary hardness of the synthesized MMNC at the disk edges of the Al-Mg produced by the HPT mechanical bonding. The Hall-Petch strengthening [31,32] due to the formation of true nano-scale grains, solid solution strengthening due to the Mg dissolution in the Al matrix during HPT and precipitation hardening when we consider the small volume of intermetallic compounds as precipitations. This evaluation specifically ignores twin boundary strengthening since there was no proof showing a presence of nanoscale twins in the Al-Mg system synthesized by HPT.

Increase in hardness by Hall-Petch strengthening and by solid solution strengthening can be estimated altogether by applying the following equation:

$$\Delta H_{HP,SS} = \frac{1}{3}[H \times (\text{wt.\% of Mg}) + kd^{-0.5}] \qquad (6)$$

where H and k are constants determined experimentally and take the values as 13.8-15.5 for Al-Mg alloys [109,110] and ~0.2 $MN \cdot m^{-3/2}$ [110], respectively, based on the relationship between hardness and yield strength under a plastic deformation stage, $H = \sigma_y/3$ (MPa) [111]. On the other hand, the precipitation hardening (Orowan hardening) in nanocrystalline metals, ΔH_p, can be described as the following relationship [112]

$$\Delta H_p = \frac{Gb}{\pi}\left\{\frac{1}{d(1-\sqrt{f}}\left[\frac{d(\sqrt{f}}{d_p}\ln\frac{d_p}{r_0}+\ln d\right]-\frac{1}{d}\ln\frac{d}{r_0}\right\} \qquad (7)$$

where d_p and f are the size and fraction of the β-Al_3Mg_2 precipitates, r_0 is the core-cutoff radius in the dislocation line energy of ~1 nm, and *G* and *b* are the shear modulus and the Burgers vector of Al as the matrix, respectively, by taking the parameters from the literature [113] and dislocation forest strengthening by the particles is included in this relationship. In this calculation, the size of the β-Al_3Mg_2 precipitates, d_p, was determined as the thickness of the β-Al_3Mg_2 thin layers observed in the TEM micrographs taken for the Al-Mg alloy after 5-10 HPT turns. Figure 5.1.1 displays the hardness improvement at the disk edge of the Al-Mg system after HPT for 10 turns which are influenced by three separate strengthening mechanisms based on eqs (6) and (7) and the total estimated hardness with increasing Mg contents in Al solid solution in wt.% [74].

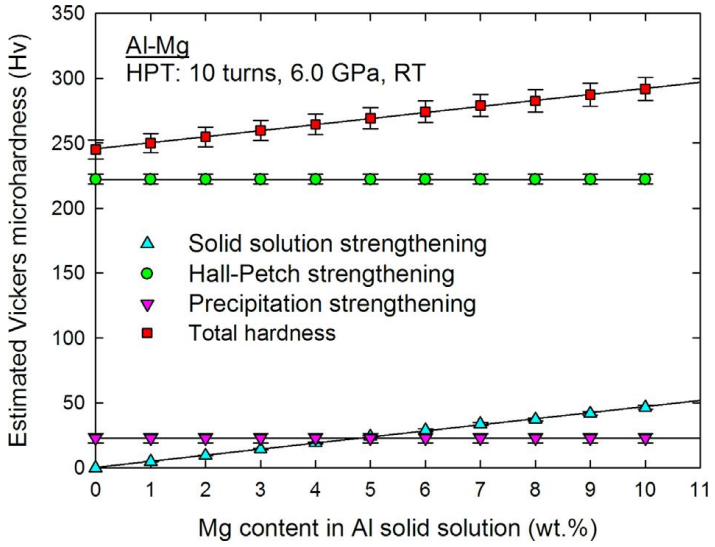

Figure 5.1.1 Estimated Vickers microhardness values with increasing Mg content in Al matrix of the Al-Mg system with 10 mm diameter after HPT for 10 turns; the red squares with error bar denotes the estimated total hardness, and the increase in hardness induced by three different strengthening mechanisms of solid solution strengthening [109,110], HP strengthening [110] and precipitation strengthening [112] are denoted by the blue upright triangles, green circles and pink inverted triangles with error bars, respectively [74]

It should be noted that the calculated hardness in MPa scale by eqs (6) and (7) was then converted to the Vickers microhardness values and also applied to Fig. 5.1.1. in order to compare those with the experimental hardness values reported in the Result section for the Al-Mg system after HPT for 5-10 turns. Thus, the estimated total hardness for the disk after 10 turns is Hv ≈ 269 ± 8 by applying the experimentally observed results, such as ~5 wt.% of Mg in the Al-SSSS, $d \approx 90$ nm, $d_p \approx 30$ nm and f <0.05. Moreover, the estimated hardness values for the disk after 5 turns is 153 ± 10 by taking ~0.5 wt.% of Mg in the Al matrix, $d \approx 190$ nm, $d_p \approx 20$ nm and f <0.05. The estimated hardness values are in excellent agreement with the Hv values recorded by the Vickers microhardness measurements of ~270 and ~130 for the Al-Mg disks after HPT for 10 and 5 turns. Therefore, it implies that these three strengthening mechanisms described in eqs (6) and (7) occur simultaneously for forming the Al-Mg MMNCs in the earlier stage of HPT processing through 10 turns. The processing conditions of low processing temperatures and the short processing time result in the concurrent occurrences of the strengthening mechanisms by preventing significant microstructural recovery during the HPT mechanical-bonding process. This estimation approach does not consider the influence by the load transfer (or load bearing) [114,115] and the difference in the thermal expansion coefficient between the different phases [116-118] due to the very small amount of the intermetallic phases in the earlier stage of HPT mechanical bonding process. Nevertheless, these Hall-Petch strengthening, solid-solution strengthening and Orowan strengthening gives reasonable estimation for the hardness of the mechanically bonded Al-Mg alloy processed by HPT.

5.2 Strength-to-weight ratio of mechanically-bonded Al-Mg

In this section, one of the important mechanical properties of strength-to-weight ratio (specific strength) will be discussed for the strengthened disk edges of the Al-Mg alloy after HPT by evaluating the improved hardness in terms of the change in an essential physical property of density. Thus, the estimation of the strength-to

weight ratios was conducted by measuring the density of the Al-Mg disk edges where MMNCs are formed after HPT for 5, 10 and 20 turns as well as the base metals for comparison purposes and by computing the values with the measured Vickers microhardness which are converted to the yield strength. The measured density, recorded Vickers microhardness values and the estimated strength-to-weight ratio are summarized in Table 4 [119]. It should be noted that the data for the base materials of Al (Al-1050) and Mg (ZK60A) in this estimation are in the ultrafine-grained condition where the saturated high hardness are achieved after HPT for 5 turns. The densities are calculated directly from the weight and volume of the disk edges.

Table 4. The measured density, the maximum Vickers microhardness value, and the estimated strength-to-weight ratio for the MMNCs in the Al-Mg system after HPT for 5-20 turns and the reference materials of Al-1050 and ZK60A alloys after 5 HPT turns. [119]

Materials	Density ($g \cdot cm^{-3}$)	Maximum hardness (Hv)	Strength-to-weight ratio ($MPa \cdot cm^{3} \cdot g^{-1}$)
MMNC after 5 HPT turns	2.50	130[74]	170
MMNC after 10 HPT turns	2.48	270[74]	350
MMNC after 20 HPT turns	2.34	330[77]	455
Al-1050 alloy after 5 turns	2.73	65[51]	80
ZK60A alloy after 5 turns	1.84	110[52]	90

There is an interesting feature in the density change of the MMNCs in the Al-Mg system where the density decreases with severe mixture of Al and Mg by increasing HPT turns. Since the densities of the base materials remain constant after HPT, the mechanical bonding of dissimilar metals by HPT shows a feasibility to synthesize the lightweight hybrid alloy systems. The changes in density of the MMNCs are caused by the diffusion bonding of dissimilar metals of Al and Mg leading to the dissolution of Mg into the Al matrix and the formation of intermetallic compounds having low densities (such as ~2.25 $g \cdot cm^{-3}$ for β-Al_3Mg_2 [120]). As a result of the lowered density, the MMNCs at the disk edge in the Al-Mg system show

exceptional strength-to-weight ratios of 350 and 455 MPa·cm^3·g^{-1} after HPT for 10 and 20 turns, respectively. These values are significantly higher than the densities of 80 and 190 MPa·cm^3·g^{-1} for the base metals of Al-1050 and ZK60A after nanostructuring by HPT. The achieved extreme strength-to-wright ratios are much higher than some steels showing ~150 MPa·cm^3·g^{-1} for structural applications and similar to the engineering polymeric composites, ceramics and carbon fibers showing ~200 MPa·cm^3·g^{-1} or higher depending on the specific applications [1].

5.3 Severe mixture of dissimilar metals during HPT

In this study, a hybrid Al-Mg system was processed by mechanical bonding of separate Al and Mg through HPT with applying a unique sample setup. Severe mixture of the dissimilar metal phases was successfully achieved with introducing nano-layered intermetallic phases, thus synthesizing MMNCs, at the disk peripheral regions and a multi-layered microstructure at the disk centers in the Al-Mg system after HPT for 5-60 turns.

It was observed in macro-scale microstructural analysis that the regions of severe mixture of dissimilar phases at the disk edges gradually expand with an increasing number of HPT turns. A similar trend was observed in the Al-Cu [81] and Zn-Mg [85] systems reported earlier. A series of these reports suggest an ability of HPT mechanical bonding to form hybrid metal solids having homogenous microstructure and mechanical properties throughout the disk volume only if high enough torsional strain is applied under high compressive pressure. Therefore, it is reasonable to investigate in macro-scale the evolution of severe mixture of metal phases during the mechanical-bonding by HPT. Specifically, a shrinkage of the layered microstructure at the disk centers are examined with an increasing number of HPT turns in the Al-Mg and Al-Cu systems.

The boundary dividing the severely mixed region at the disk edges and the layered microstructure at the central regions is described by the distance from the disk center, r_b, where sudden hardness increases often appear in the hardness contour maps

and disappearances of dark Mg- and Cu-rich phases occurs within the Al matrix at the cross-sectional surfaces of the Al-Mg [78] and Al-Cu [81] systems. Figure 5.3.1 represents the trends of the severe phase mixture during HPT mechanical bonding by showing r_b and the corresponding equivalent strain and the shear strain applied to the materials at the specific locations for both Al-Mg and Al-Cu systems after HPT for up to 60 turns under 6.0 GPa at 1.0 rpm [78]. The plot includes a linear regression to better visualize the relationship between r_b and the estimated equivalent strain and the shear strain for each material system. A disk thickness of h = 0.7-0.8 mm was applied for calculating the equivalent strain and shear strain where the disk thickness before HPT of ~2.4 mm was reduced to <0.8 mm after compression and an early stage of torsional straining and thereafter remained reasonably constant as shown in Fig. 4.1.1 and the literature [81].

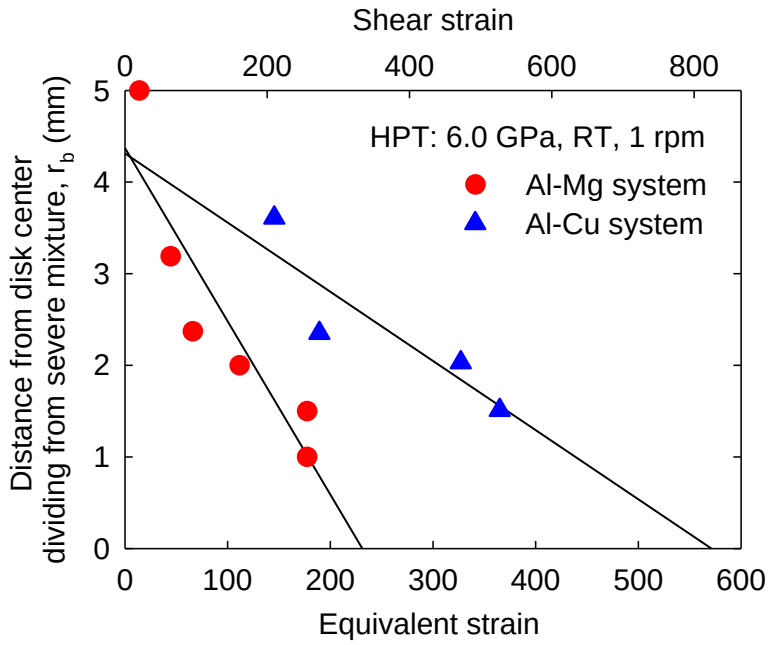

Figure 5.3.1 A relationship between r_b and the estimated shear strain and equivalent strain for both Al-Mg and Al-Cu systems after HPT for up to 60 turns and up to 40 turns, respectively, under 6.0 GPa for 1.0 rpm at RT [78]

There are two important findings that should be discussed in Fig. 5.3.1. First, there are linear relationships between r_b and the imposed strain for both Al-Mg and Al-Cu systems, while there is a difference in the slope of the linear regressions which implies that the required applied strain for synthesizing the severe metal mixture by HPT depends on the materials selection. It is suggested earlier by cladding of dissimilar metal plates by simple rolling that a reduction in the hardness difference between the selected dissimilar metals improves the bonding of the metals [121]. Applying this approach, a difference in hardness between the dissimilar metals is higher for the Al-Cu system than the Al-Mg system. Subsequently, the trend of the expansion of the severe phase mixture by HPT shows the Al-Cu system requires higher torsional strain by applying higher HPT turns in comparison with the Al-Mg system that requires lower numbers of HPT turns for demonstrating the consistent level of severe phase mixture.

Secondly, the linear relationship between r_b and the imposed strain in Fig. 5.3.1 anticipates the feasibility of HPT mechanical bonding for achieving homogeneous microstructure, thus hardness, across the disk diameters of the Al-Mg and Al-Cu systems when higher numbers of HPT than 60 are applied. In practice, in order to reduce the central regions containing the multi-layered microstructure at r_b <0.5 mm, total equivalent strains of ~230 and ~570, which are equivalent to 80 turns and 140 turns, are required for the Al-Mg and Al-Cu systems, respectively. In this context, a very recent preliminary trial of HPT-induced mechanical bonding demonstrated the homogeneous microstructure of the Al-Mg system after the mechanical bonding through HPT for 100 turns under 6.0 GPa at 1.0 rpm [80]. Consequently, it is suggested the application of HPT turns more than the suggested numbers may obtain a homogeneous bulk nanostructured metal system through the HPT-induced mechanical bonding and further experiments are necessary for understanding this microstructural evolution with applying a variety of metal combinations.

It should be noted that there may be additional factors affecting the solid-state reaction of dissimilar metals, such as a small heat generation during HPT [122], actual applied pressure within the materials when applying different numbers of disks [82], and the sample size effect which was shown in Fig. 4.2.3.

6. Summary and conclusions

(1) The mechanical bonding of separate Al and Mg disks was successfully demonstrated using conventional HPT processing with a unique sample set-up for introducing a hybrid Al-Mg system. For processing of 10 mm diameter disks, HPT was conducted under 6.0 GPa at 1.0 rpm up to 60 turns at RT. For 25 mm diameter disks, processing was operated under 1.0 GPa at 0.25 rpm up to 20 turns at RT. PDA was conducted for the Al-Mg disk with 10 mm diameter after 20 HPT turns at 573 K for 1 h in order to evaluate the hardness and microstructural stability.

(2) A multi-layered structure in the order of Al/Mg/Al was observed along the disk diameter after 1 turn and it remained at the central regions after HPT up to 60 turns for the disk having 10 mm diameter. The peripheral regions showed a single phase-like microstructure after HPT for 10 turns and higher whereas fine Mg phases are homogeneously distributed at the disk edge after HPT for 5 turns.

(3) A true nano-scale microstructure was observed with average grain sizes of ~190 nm, ~90 nm and ~60 nm at the disk edges of the disk having 10 mm diameter after 5, 10 and 20 turns, respectively. After 20 turns followed by PDA, an equiaxed microstructure was achieved with an average grain size of ~380 nm at the peripheral region. A detailed compositional analysis demonstrated the formation of different types of MMNCs at the peripheries of the disks after processing by HPT and processing followed by PDA. In practice, an intermetallic compound of β-Al_3Mg_2 was observed with a layer thickness of ~20 nm in the Al matrix after 5 turns. After 10 and 20 turns, two intermetallic compounds of β-Al_3Mg_2 and γ-$Al_{12}Mg_{17}$ were observed without any Mg-rich phases in the matrix. The disk after 20 turns followed by PDA showed the presence of an Al-7% Mg phase in addition to the two intermetallic compounds.

(4) Significant grain refinement and the severe mixture of metal phases demonstrated significantly high Vickers microhardness of ~270 and ~330 and thus exceptional specific strength of ~350 $MPa \cdot cm^3 \cdot g^{-1}$ and ~455 $MPa \cdot cm^3 \cdot g^{-1}$ at the disk edges after HPT for 10 and 20 turns, respectively, due to the lightweighting of the

alloy system by the severe mixture of dissimilar metal phases. The Vickers hardness was reduced to Hv ≈ 220 after PDA. The simultaneous occurrence of HP strengthening, sold solution strengthening and precipitation hardening attributes to the exceptional hardness at the disk edges of the synthesized MMNCs after HPT.

(5) After additional torsional strains by 40-60 turns, exceptional hardness of Hv ≈ 330 appeared in the widened regions of the Al-Mg alloy disks with 10 mm dimeter. Microstructural analysis by utilizing μXRD and MAUD estimated the crystallite sizes of 40 and 30 nm containing a super saturated Al-rich phase without any Mg-rich and intermetallic phases after 40 and 60 turns, respectively.

(6) The region of the sample disk edges having severe mixture of dissimilar metals expand linearly with increasing torsional straining. Thus, there is a potential for synthesizing a hybrid alloy system having a homogenous microstructure throughout the disks by HPT when the large enough torsional strain is applied in the Al-Mg and Al-Cu systems.

(7) The scaled-up Al-Mg disks having 25 mm diameter show a general hardness distribution for HPT processed disks where the highest hardness was recorded at the disk peripheries and decreases toward to the centers of the disks. The maximum hardness was recorded as Hv ≈ 250 at the disk edge after HPT for 20 turns and an average grain size of ~380 nm was observed by TEM in the corresponding area.

(8) Microstructural heterogeneity was observed in the mechanically bonded Al-Mg system with 25 mm dimeter through μXRD and MAUD analysis by computing the lattice parameter of Al and coherent crystallite size in several different locations within the disks after HPT for 10 and 20 turns.

(9) The experimental results demonstrated the feasibility of processing dissimilar metals by using a conventional HPT processing for developing new lightweight alloy systems having exceptional properties. By considering the scaling-up of the samples, mechanical bonding of dissimilar metals by HPT provides excellent

contributions to current manufacturing techniques in diffusion bonding, welding and mechanical joining.

7. Future work

- Synthesis of a series of bulk metastable Al alloys will be demonstrated by the mechanical bonding of dissimilar metals through the application of HPT processing
- The materials processed by HPT demonstrate heterogeneity in texture, phase transformation and composition even after reasonable microstructural homogeneity is achieved throughout the disk volume. Advanced characterization techniques such as high-energy X-ray, neutron and synchrotron diffraction analyses were applied in addition to the series of lab-scale XRD analysis.

(1) Synchrotron diffraction experiments were conducted for various HPT processed materials at room temperature at a beam line of BL02B1 in Spring-8, Japan on February 2019.

(2) A series of data should be analyzed mainly for evaluating the heterogeneity in texture, phase transformation and composition of the HPT-processed materials including Al-Mg and TiAl intermetallic compounds.

- Neutron diffraction experiments will be conducted for a series of HPT samples including the Al-Mg mechanically bonded material to investigate the phase stability, phase transformation and new phase nucleation at in-situ high temperature heating at Japan Proton Accelerator Research Complex (J-PARC), Japan, on 12-15 February 2020.

Bibliography

[1] K. Lu, Science 328 (2010) 319.
[2] R.Z. Valiev, Y. Estrin, Z. Horita, T.G. Langdon, M.J. Zehetbauer, Y.T. Zhu, JOM 58(4) (2006) 33.
[3] R.Z. Valiev, Y. Estrin, Z. Horita, T.G. Langdon, M.J. Zehetbauer, Y.T. Zhu, JOM 68 (2016) 1216.
[4] R.Z. Valiev, Y. Estrin, Z. Horita, T.G. Langdon, M.J. Zehetbauer, Y.T. Zhu, Mater. Res. Lett. 4 (2016) 1.
[5] A.P. Zhilyaev, T.G. Langdon, Prog. Mater. Sci. 53 (2008) 893.
[6] T.G. Langdon, Acta Mater. 61 (2013) 7035.
[7] P.V. Liddicoat, X.Z. Liao, Y.T. Zhu, Y.H. Zhao, E.J. Lavernia, M.Y. Murashkin, R.Z. Valiev, S.P. Ringer, Nat. Commun. 1 (2010) 63.
[8] R.Z. Abdulov, R.Z. Valiev, N.A. Krasilnikov, J. Mater. Sci. Lett. 9 (1990) 1445.
[9] A.V. Korznikov, O. Dimitrov, G.F. Korznikova, J.P. Dallas, A. Quivy, R.Z. Valiev, A. Mukherjee, Nanostruct. Mater. 11 (1999) 17.
[10] N.V. Kazantseva, N.V. Mushnikov, A.G. Popov, P.B. Terent'ev, V.P. Pilyugin, J. Alloys. Compd. 509 (2011) 9307.
[11] B. Srinivasarao, A.P. Zhilyaev, R. Muñoz-Moreno, M.T. Pérez-Prado, J. Mater. Sci. 48 (2013) 4599.
[12] J.-K. Han, X. Li, R. Dippenaar, K.-D. Liss, M. Kawasaki, Mater. Sci. Eng. A 714 (2018) 84.
[13] R. Pippan, F. Wetscher, M. Hafok, A. Vorhauer, I. Sabirov, Adv. Eng. Mater. 8 (2006) 1046.
[14] S. Sabbaghianrad, T.G. Langdon, Mater. Sci. Eng. A 596 (2014) 52.
[15] P. Bazarnika, Y. Huang, M. Lewandowska, T.G. Langdon, Mater. Sci. Eng. A 712 (2018) 513.
[16] X. Sauvage, G. Wilde, S.V. Divinski, Z. Horita, R.Z. Valiev, Mater. Sci. Eng. A 540 (2012) 1.
[17] A.P. Zhilyaev, A.A. Gimazov, G.I. Raab, T.G. Langdon, Mater. Sci. Eng. A 486 (2008) 123.
[18] K. Edalati, Y. Yokoyama, Z. Horita, Mater. Trans. 51 (2010) 23.
[19] M.I. Abd El Aal, E.Y. Yoon, H.S. Kim, Mater. Sci. Eng. A 560 (2013) 121.
[20] M.M. Castro, P.H.R. Pereira, A. Isaac, R.B. Figueiredo, T.G. Langdon, J. Alloys Compd. 780 (2019) 422.
[21] A.V. Korznikov, I.M. Safarov, D.V. Laptionok, R.Z. Valiev, Acta Metall. Mater. 39 (1991) 3193.
[22] V.V. Stolyarov, Y.T. Zhu, T.C. Lowe, R.K. Islamgaliev, R.Z. Valiev, Mater. Sci. Eng. A 282 (2000) 78.
[23] X. Sauvage, P. Jessner, F. Vurpillot, R. Pippan, Scr. Mater. 58 (2008) 1125.
[24] K. Kaneko, T. Hata, T. Tokunaga, Z. Horita, Mater. Trans. 50 (2009) 76.

[25] K. Edalati, Z. Horita, H. Fujiwara, K. Ameyama, Metall. Mater. Trans. A 41A (2010) 3308.
[26] A. Bachmaier, M. Kerber, D. Setman, R. Pippan, Acta Mater. 60 (2012) 860.
[27] J.M. Cubero-Sesin, Z. Horita, Mater. Sci. Eng. A 558 (2012) 462.
[28] Y. Zhang, S. Sabbaghianrad, H. Yang, T.D. Topping, T.G. Langdon, E.J. Lavernia, J.M. Schoenung, S.R. Nutt, Metall. Mater. Trans. A 46A (2015) 5877.
[29] A.P. Zhilyaev, G. Ringot, Y. Huang, J.M. Cabrera, T.G. Langdon, Mater. Sci. Eng. A 688 (2017) 498.
[30] Y. Huang, P. Bazarnik, D. Wan, D. Luo, P.H.R. Pereira, M. Lewandowska, J. Yao, B.E. Hayden, T.G. Langdon, Acta Mater. 164 (2019) 499.
[31] E.O. Hall, Proc. Phys. Soc. B 64 (1951) 747.
[32] N.J. Petch, J. Iron Steel Inst. 173 (1953) 25.
[33] H. Gleiter, Prog. Mater. Sci. 33 (1989) 223.
[34] R.A. Masumura, P.M. Hazzledine, C.S. Pande, Acta Metall. 46 (1998) 4527.
[35] L.K.L. Falk, P.R. Howell, G.L. Dunlop, T.G. Langdon, Acta Metall. 34 (1986) 1203.
[36] Z.N. Farhat, Y. Ding, D.O, Northwood, A.T. Alpas, Mater. Sci. Eng. A 206 (1996) 302.
[37] D.H. Jeong, F. Gonzalez, G. Palumbo, K.T. Aust, U. Erb. Scripta Mater. 44 (2001) 493.
[38] R.Z. Valiev, M.Y. Murashikin, I. Sabirov, Scr. Mater. 76 (2014) 13.
[39] R.Z. Valiev, Nature Mater. 3 (2004) 511.
[40] Y.T. Zhu, R.Z. Valiev, T.G. Langdon, N. Tsuji, K. Lu, MRS Bull. 35 (2010) 977.
[41] R.Z. Valiev, T.G. Langdon, Metall. Mater. Trans. A 42A (2011) 2942.
[42] R.Z. Valiev, T.G. Langdon, Prog. Mater. Sci. 51 (2006) 881.
[43] Y. Iwahashi, J. Wang, Z. Horita, M. Nemoto, Scr. Mater. 35 (1996) 143.
[44] Y. Saito, H. Utsunomiya, N. Tsuji, T. Sakai, Acta Mater. 47 (1999) 579.
[45] P.W. Bridgman, J. Appl. Phys. 14 (1943) 273.
[46] K. Edalati, Z. Horita, Mater. Sci. Eng. 652 (2016) 325.
[47] A.P. Zhilyaev, T.R. McNelley, T.G. Langdon, J. Mater. Sci. 42 (2007) 1517.
[48] C. Xu, Z. Horita, T.G. Langdon, Acta Mater. 56 (2008) 5168.
[49] A.P. Zhilyaev, G.V. Nurislamova, B.K. Kim, M.D. Baró, J.A. Szpunar, T.G. Langdon, Acta Mater. 51 (2003) 753.
[50] R.Z. Valiev, Y.V. Ivanisenko, E.F. Rauch, B. Baudelet, Acta Mater. 44 (1996) 4705
[51] M. Kawasaki, S.N. Alhajeri, C.Xu, T.G. Langdon, Mater. Sci. Eng. A 529 (2011) 345.
[52] H.-J. Lee, S.K. Lee, K.H. Jung, G.A. Lee, B. Ahn, M. Kawasaki, T.G. Langdon, Mater. Sci. Eng. A 630 (2015) 90.
[53] M. Kawasaki, J. Mater. Sci. 49 (2014) 18.
[54] R.Z. Valiev, I.V. Alexandrov, Y.T. Zhu, T.C. Lowe, J. Mater. Res. 17 (2002) 5.

[55] R.Z. Valiev, Nature, 419 (2002) 887.
[56] R.Z. Valiev, Nat. Mater. 3 (2004) 511.
[57] P. Kumar, M. Kawasaki, T.G. Langdon, J. Mater. Sci. 51 (2016) 7.
[58] Y.T. Zhu, X.Z. Liao, X.L. Wu, Prog. Mater. Sci. 57 (2012) 1.
[59] D. Jia, Y.M. Wang, K.T. Ramesh, E. Ma, Y.T. Zhu, R.Z. Valiev, Appl. Phys. Lett. 79 (2001) 611.
[60] Y.M. Wang, E. Ma, Mater. Sci. Eng. A 375–377 (2004) 52.
[61] Y.T. Zhu, X. Liao, Nat. Mater. 3 (2004) 351.
[62] T. Mungole, P. Kumar, M. Kawasaki, T.G. Langdon, J. Mater. Res. 29 (2014) 2534.
[63] H. Chang, M.Y. Zheng, C. Xu, G.D. Fan, H.G. Brokmeier, K. Wu, Mater. Sci. Eng. A 543 (2012) 249.
[64] A. Macwan, X.Q. Jiang, C. Li, D.L. Chen, Mater. Sci. Eng. A 587 (2013) 344.
[65] M. Eizadjou, A.K. Talachi, H.D. Manesh, H.S. Shahabi, K. Janghorban, Compos. Sci. Technol. 68 (2008) 2003.
[66] V.Y. Mehr, M.R. Toroghinejad, A. Rezaeian, Mater. Sci. Eng. A 601 (2014) 40.
[67] M.C. Chen, H.C. Hsieh, W. Wu, J. Alloy. Compd. 416 (2006) 169.
[68] M.C. Chen, C.W. Kuo, C.M. Chang, C.C. Hsieh, Y.Y. Chang, W. Wu, Mater. Trans. 48 (2007) 2595.
[69] N. Chang, M.Y. Zheng, C. Xu, G.D. Fan, H.G. Brokmeier, K. Wu, Mater. Sci. Eng. A 543 (2012) 249.
[70] R.N. Dehsorkhi, F. Qods, M. Tajally, Mater. Sci. Eng. A 530 (2011) 63.
[71] B. Beausir, J. Scharnweber, J. Jaschinski, H.-G. Brokmeier, C.-G. Oertel, W. Skrotzki, Mater. Sci. Eng. A 527 (2010) 3271.
[72] K. Oh-ishi, K. Edalati, H.S. Kim, K. Hono, Z. Horita, Acta Mater. 61 (2013) 3482.
[73] O. Bouaziz, H.S. Kim, Y. Estrin, Adv. Eng. Mater. 15 (2013) 336.
[74] B. Ahn, A.P. Zhilyaev, H.-J. Lee, M. Kawasaki, T.G. Langdon, Mater. Sci. Eng. A 635 (2015) 109.
[75] B. Ahn, H.-J. Lee, I.C. Choi, M. Kawasaki, J.-i. Jang, T.G. Langdon, Adv. Eng. Mater. 18 (2016) 1001.
[76] M. Kawasaki, B. Ahn, H.-J. Lee, A.P. Zhilyaev, T.G. Langdon, J. Mater. Res. 31 (2016) 88.
[77] J.-K. Han, H.-J. Lee, J.-i. Jang, M. Kawasaki, T.G. Langdon, Mater. Sci. Eng. A 684 (2017) 318.
[78] M. Kawasaki, S.-H. Jung, J.-M. Park, J. Lee, J.-i. Jang, J.-K. Han, Adv. Eng. Mater. 2019 (in press). DOI: 10.1002/adem.201900483
[79] J.-K. Han, J.-M. Park, W. Ruan, K.T. Carpenter, A. Tabei, J.-i. Jang, M. Kawasaki, Adv. Eng. Mater. 2019, DOI: 10.1002/adem.201900971
[80] J.-K. Han, K.-D. Liss, T.G. Langdon, M. Kawasaki, Sci. Rep. (under review)
[81] J.-K. Han, D.K. Han, G.Y. Liang, J.-i. Jang, T.G. Langdon, M. Kawasaki, Adv. Eng. Mater. 20 (2018) 1800642.

[82] M. Kawasaki, J.-K. Han, D.-H. Lee, J.-i. Jang, T.G. Langdon, J. Mater. Res. 33 (2018) 2700.
[83] V.N. Danilenko, S.N. Sergeev, J.A. Baimova, G.F. Korznikova, K.S. Nazarov, R.Kh. Khisamov, A.M. Glezer, R.R. Mulyukov, Mater. Lett. 236 (2019) 51.
[84] Y. Qi, A. Kosinova, A.R. Kilmametov, B.B. Straumal, E.Rabkin, Mater. Charact. 145 (2018) 389.
[85] D. Hernández-Escobar, Z.U. Raman, H. Yilmazer, M. Kawasaki, C.J. Boehlert, Phil. Mag. 99 (2019) 557.
[86] S.O. Rogachev, R.V. Sundeev, V.M. Khatkevich, Mater. Lett. 173 (2016) 123.
[87] S.O. Rogachev, S.A. Nikulin, A.B. Rozhnov, V.M. Khatkevich, T.A. Nechaykina, M.V. Gorshenkov, R.V. Sundeev, Metall. Mater. Trans. A 48A (2017) 6091.
[88] S.O. Rogachev, R.V. Sundeev, N.Yu. Tabachkova, Mater. Lett. 234 (2019) 220.
[89] R.B. Figueiredo, P.R. Cetlin, T.G. Langdon, Mater. Sci. Eng. A 528 (2011) 8198.
[90] R.B. Figueiredo, P.H.R. Pereira, M.T.P. Aguilar, P.R. Cetlin, T.G. Langdon, Acta Mater. 60 (2012) 3190.
[91] M. Kawasaki, T.G. Langdon, Mater. Sci. Eng. A 498 (2008) 341.
[92] L. Lutterotti, Nucl. Instrum. Methods Phys. Res. Sect. B 268 (2010) 334.
[93] M. Kawasaki, J.-i. Jang, Materials 10(6) (2017) 596.
[94] F. Wetscher, A. Vorhauer, R. Stock, R. Pippan, Mater. Sci. Eng. A 387–389 (2004) 809.
[95] F. Wetscher, R. Pippan, S. Sturm, F. Kauffmann, C. Scheu, G. Dehm, Metall. Mater. Trans. A 37A (2006) 1963.
[96] L. Vegard, Z. Physik 5 (1921) 17.
[97] L. Vegard, H. Dale, Z. Kristallogr. 67 (1928) 148.
[98] H.L. Luo, C.C. Chao, P. Duwez, Trans. Metall. Soc. AIME 230 (1964) 1488.
[99] M. Schoenitz, E.L. Dreizin, J. Mater. Res. 18 (2003) 1827.
[100] H. Okamoto, J. Phase Equilib. 19 (1998) 598.
[101] X. Sauvage, N. Enikeev, R. Valiev, Y. Nasedkina, M. Murashkin, Acta Mater. 72 (2014) 125.
[102] H.-J. Lee, J.-K. Han, S. Janakiraman, B. Ahn, M. Kawasaki, T.G. Langdon, J. Alloy. Compd. 686 (2016) 998
[103] S.V. Divinski, J. Ribbe, D. Baither, G. Schmitz, G. Reglitz, H. Rösner, K. Sato, Y. Estrin, G. Wilde, Acta Mater. 57 (2009) 5706.
[104] S.V. Divinski, G. Reglitz, H. Rösner, Y. Estrin, G. Wilde, Acta Mater. 59 (2011) 1974.
[105] D.-H. Lee, I.-C. Choi, M.-Y. Seok, J. He, Z. Lu, J.-Y. Suh, M. Kawasaki, T.G. Langdon, J.-i. Jang, J. Mater. Res. 30 (2015) 2804.
[106] Y. Huang, M. Kawasaki, T.G. Langdon, J. Mater. Sci. 48 (2013) 4533.
[107] G.K. Williamson, W.H. Hall, Acta Metall. 1 (1953) 22.
[108] E.J. Mittemeijer, U. Welzel, Z. Kristallogr. Cryst. Mater. 223 (2008) 552.

[109] T. Mukai, K. Higashi, S. Tanimura, Mater. Sci. Eng. A 176 (1994) 181.
[110] G.B. Burger, A.K. Gupta, P.W. Jeffrey, D.J. Lloyd, Mater. Charact. 35 (1995) 23.
[111] S. Shim, J.-i. Jang, G.M. Pharr, Acta Mater. 56 (2008) 3824–3832.
[112] K.V. Rajulapati, R.O. Scattergood, K.L. Murty, Z. Horita, T.G. Langdon, C.C. Koch, Metall. Mater. Trans. A 39A (2008) 2528.
[113] W.S. Miller, F.J. Humphreys, Scr. Metall. Mater. 25 (1991) 33.
[114] S.M. Uddin, T. Mahmud, C. Wolf, C. Glanz, I. Kolaric, C. Volkmer, H. Höller, U. Wienecke, S. Roth, H. Fecht, Compos. Sci. Technol. 55 (2010) 42.
[115] R. Casati, M. Vedani, Metals 4 (2014) 65.
[116] W.S. Miller, F.J. Humphreys, Scr. Metall. Mater. 25 (1991) 33.
[117] R.J. Arsenault, Mater. Sci. Eng. 81 (1986) 175.
[118] R.J. Arsenault, L. Wang, C.R. Feng, Acta Metall. Mater. 39 (1991) 47.
[119] M. Kawasaki, T.G. Langdon, Mater. Res. 20(Suppl.1) (2017) 46.
[120] S. Samson, Acta Crystallogr. 19 (1965) 401.
[121] L. Li, K. Nagai, F. Yin, Sci. Technol. Adv. Mater. 9 (2008) 023001
[122] K. Edalati, Y. Hashiguchi, P.H.R. Pereira, Z. Horita, T.G. Langdon, Mater. Sci. Eng. A 714 (2018) 167.